

RESEARCH

Open Access



# Pulmonary mitochondrial DNA release and activation of the cGAS-STING pathway in Lethal *Stx12* knockout mice

Dan-Hua Liu<sup>1,2,3</sup>, Fang Li<sup>4</sup>, Run-Zhou Yang<sup>1</sup>, Zhuabin Wu<sup>5</sup>, Xiao-Yan Meng<sup>1,2,3</sup>, Sen-Miao Li<sup>1,2,3</sup>, Wen-Xiu Li<sup>1,2,3</sup>, Jia-Kang Li<sup>1,2,3</sup>, Dian-Dian Wang<sup>1,2,3</sup>, Rui-Yu Wang<sup>1,2,3</sup>, Shu-Ang Li<sup>1</sup>, Pei-Pei Liu<sup>1</sup> and Jian-Sheng Kang<sup>1,2,3\*</sup>

## Abstract

STX12 (syntaxin12 or syntaxin13), a member of the SNARE protein family, plays a crucial role in intracellular vesicle transport and membrane fusion. Our previous research demonstrated that *Stx12* knockout mice exhibit perinatal lethality with iron deficiency anemia. Despite its importance, the comprehensive physiological and pathological mechanism of STX12 remains largely unknown. Here, we revealed that STX12 deficiency causes the depolarization of mitochondrial membrane potential in zebrafish embryos and mouse embryonic fibroblasts. Additionally, the loss of STX12 decreased the levels of mitochondrial complex subunits, accompanied by mitochondrial DNA (mtDNA) release and activated cGAS-STING pathway and Type I interferon pathway in the lung tissue of *Stx12*<sup>-/-</sup> mice. Additionally, we observed a substantial increase in cytokines and neutrophil infiltration within the lung tissues of *Stx12* knockout mice, indicating severe inflammation, which could be a contributing factor for *Stx12*<sup>-/-</sup> mortality. Various interventions have failed to rescue the lethal phenotype, suggesting that systemic effects may contribute to lethality. Further research is warranted to elucidate potential intervention strategies. Overall, our findings uncover the critical role of STX12 in maintaining mitochondrial function and mtDNA stability in pulmonary cells, and reveal that STX12 depletion results in pulmonary mtDNA release and activates mtDNA-dependent innate immunity.

**Keywords** cGAS-STING, Inflammation, Mitochondria, mtDNA release, STX12

## Introduction

Soluble N-ethylmaleimide-sensitive factor attachment protein receptors (SNAREs) are a family of proteins that play crucial roles in the process of membrane fusion within eukaryotic cells [1, 2]. They are essential for various

cellular functions, including vesicle trafficking, neurotransmitter release [3, 4], and the fusion of transport vesicles with their target membranes. Syntaxin 12 (STX12) is a member of the Qa-SNARE protein family, which plays a critical role in the endosomal trafficking pathway, where it facilitates the sorting and recycling of endocytosed materials [5–7]. The expression of STX12 is reported to be developmentally regulated and is abundant during the late embryonic and early postnatal phases, with levels subsequently diminishing as the brain matures into the late postnatal stages in the mice and rats [8, 9]. Additionally, in primary cultured neurons and differentiated PC12 cells, STX12 is prominently found in the perinuclear area of the cell body, as well as distributed along neurites and within growth cones [9, 10]. The overexpression of STX12 in

\*Correspondence:

Jian-Sheng Kang  
kjs@zzu.edu.cn

<sup>1</sup> Clinical Systems Biology Laboratories, The First Affiliated Hospital of Zhengzhou University, Zhengzhou, China

<sup>2</sup> Department of Neurology, The First Affiliated Hospital of Zhengzhou University, Zhengzhou, China

<sup>3</sup> The First Clinical College, Zhengzhou University, Zhengzhou, China

<sup>4</sup> Department of Anesthesiology, Shanghai General Hospital, Shanghai Jiao Tong University School of Medicine, Shanghai, China

<sup>5</sup> Shanghai Model Organisms Center, Inc., Shanghai, China



© The Author(s) 2025. **Open Access** This article is licensed under a Creative Commons Attribution-NonCommercial-NoDerivatives 4.0 International License, which permits any non-commercial use, sharing, distribution and reproduction in any medium or format, as long as you give appropriate credit to the original author(s) and the source, provide a link to the Creative Commons licence, and indicate if you modified the licensed material. You do not have permission under this licence to share adapted material derived from this article or parts of it. The images or other third party material in this article are included in the article's Creative Commons licence, unless indicated otherwise in a credit line to the material. If material is not included in the article's Creative Commons licence and your intended use is not permitted by statutory regulation or exceeds the permitted use, you will need to obtain permission directly from the copyright holder. To view a copy of this licence, visit <http://creativecommons.org/licenses/by-nc-nd/4.0/>.

PC12 cells can enhance neurite outgrowth during nerve-growth-factor-induced differentiation [9, 11]. STX12 is also involved in autophagosome maturation as a genetic modifier of mutant CHMP2B in frontotemporal dementia [12]. Studies have shown that STX12 colocalizes with internalized transferrin and the transferrin receptor [5]. Our previous study has revealed a deficiency in fast recycling of the transferrin receptor in *Stx12*<sup>-/-</sup> MEFs, and demonstrated that *Stx12*-knockout mice exhibit iron deficiency anemia and perinatal lethality [13]. However, the pathophysiological alterations and the underlying lethal mechanism of STX12 deficiency remain unknown.

Given the perinatal lethality of *Stx12*-knockout mice and the difficulty in exploring potential mechanisms in mice, we generated *Stx12*-knockdown zebrafish to investigate the potential effects of STX12 deficiency. Our findings indicated that *Stx12* knockdown in zebrafish resulted in approximately 80% mortality rate within 6 h post-fertilization, accompanied by mitochondrial damage. Furthermore, we observed pronounced activation of inflammatory response and reductions in the expression levels of mitochondrial complex subunits in the lung tissue of *Stx12*-knockout mice. Further mechanistic studies suggested that mitochondrial DNA (mtDNA) escaped into the cytoplasm, leading to the activation of the cGAS-STING pathway and subsequently triggering the Type I interferon pathway in alveolar epithelial cells of *Stx12*-knockout mice. Notably, we discovered that this inflammatory response was closely associated with neutrophils, wherein a positive feedback loop involving neutrophil infiltration and cytokine release exacerbated the inflammation. This amplified inflammatory response is speculated to be a potential cause of perinatal mortality observed in *Stx12*-knockout mice.

## Materials and methods

### Zebrafish care and maintenance

Adult wild-type AB strain zebrafish were maintained at 28.5 °C on a 14 h light/10 h dark cycle. Five to six pairs of zebrafish were set up for natural mating each time. The embryos were maintained at 28.5 °C in fish water (0.2% Instant Ocean Salt in deionized water).

### Animal care and interventions

All animal care and experiments were performed in accordance with Institutional Animal Care and Use Committee of the first affiliated hospital of Zhengzhou University guidelines (2024-KY-0928).

*Stx12*-knockout mice were generated by inserting a EGFP gene with a stop codon 10 bp upstream of the ATG start codon of the *Stx12* gene, as previously described [13]. These mice were generated by Shanghai Model

Organisms Center, Inc. (Shanghai, China). All mice were maintained in a 12-h light–dark cycle at 22 °C.

### Zebrafish microinjections

The morpholino (MO) was designed and synthesized by Gene Tools, LLC (<http://www.gene-tools.com/>). Antisense MOs (GeneTools) were microinjected into fertilized one-cell stage embryos according to standard protocols.

*Stx12* ATG-MO 5′- TGGAGCAAACACTACAGCAG GAAGCCA –3′

*Stx12* E4I4-MO 5′- ACTGGCAACTACAAAAGTACC TGTT –3′

Control-MO 5′- CCTCTTACCTCAGTTACAATT TATA –3′

The doses of the MOs used for injection were as follows: Control-MO and E4I4-MO, 4 ng per embryo; ATG-MO, 4 ng per embryo. Primers spanning *Stx12* exon 2 and exon 3 (forward primer: 5′- CACACTGAA TACCGCTCAAATC –3′) and exon 5 (reverse primer: 5′- CCACTGACTCCTTCTCTTTCTC –3′) were used for RT-PCR analysis to verify the efficacy of the E4I4-MO.

### Acridine orange staining for apoptosis

Control-MO injected embryos and embryos injected with *Stx12*-MO were immersed in 5 µg/ml AO (acridinium chloride hemi-[zinc chloride], Sigma-Aldrich, St. Louis, MO, USA) in fish water from 2-hpf to 3.7-hpf at 28.5 °C. Next, the zebrafish embryos were rinsed thoroughly in fish water three times (5 min/wash) and then oriented on their lateral side and mounted with methylcellulose on a depression slide for observation via fluorescence microscopy.

### TMRM staining in zebrafish

The mitochondrial membrane potential ( $\Delta\Psi_m$ ) was estimated by monitoring the fluorescence intensity of tetramethylrhodamine methyl ester, perchlorate, biotium (TMRM) [14, 15]. To determine the efficacy of TMRM staining in zebrafish embryos, uninjected WT AB zebrafish embryos were immersed in four different concentrations of TMRM (0.05, 0.1, 0.3, and 1 µM) in fish water from 2 hpf to 3.7 hpf at 28.5 °C in the dark. After treatment, the embryos were checked via a Nikon SMZ18 fluorescence microscope. The results showed that 1 µM TMRM displayed a good fluorescent signal. Control-MO-injected embryos and embryos injected with *Stx12*-MO were immersed in 1 µM TMRM in fish water from 2 hpf to 3.7 hpf at 28.5 °C in the dark. Next, the zebrafish embryos were rinsed thoroughly in fish water three times (5 min/wash) at 3.7 hpf. Zebrafish embryos were then oriented on their lateral side and mounted with

methylcellulose on a depression slide for observation via fluorescence microscopy.

#### Primary culture of mouse embryo fibroblasts (MEFs)

The anesthetized pregnant mouse at embryonic 17.5 was sacrificed, and the uterus was carefully dissected. The uterus was immersed in 75% (v/v) ethanol, followed by rinsing with PBS without  $\text{Ca}^{2+}$  or  $\text{Mg}^{2+}$  (Gibco, Invitrogen, Carlsbad, CA, USA). Each embryo was separated from its placenta; the head, limbs and viscera were removed and the remaining tissue was minced into pieces as small as possible. A part of the tail was used for genotype identification. The tissues were digested in 15 ml of 0.05% trypsin at 37 °C for 30 min, and the 50 ml tube was shaken every 10 min. Trypsin activity was terminated by adding an equal volume of MEF medium (10 ml of FBS in 90 ml of DMEM). The cells were centrifuged at 1000×g for 5 min, the supernatant was discarded, and this step was repeated once. Finally, the cells were resuspended in 10 ml of MEF medium and cultured in a 55 cm<sup>2</sup> Petri dish at 37 °C with 5% CO<sub>2</sub>.

#### Cytokine array

Blood samples from *Stx12*-knockout (KO) and wild-type (WT) littermate control mice were collected via decapitation using capillary tubes, and the blood samples were allowed to clot at room temperature for 2 h. The samples were subsequently centrifuged at 2,000×g for 15 min at 4 °C to obtain the serum. Tissue samples from *Stx12*-knockout (KO) mice were collected, homogenized in lysis buffer (1% Triton X-100, 20 mM Tris-HCl pH 7.5, 150 mM NaCl, 1% deoxycholate, and protease inhibitor cocktail), and centrifuged at 12,000×g for 15 min at 4 °C. The supernatants were collected, and the protein concentrations were determined via a BCA protein assay kit (Epizyme Biotech, Shanghai, China). The cytokine profile of the tissue homogenates was assessed via the Mouse Cytokine Array Panel A (R&D Systems, Minneapolis, MN, USA) according to the manufacturer's instructions. Briefly, array membranes were blocked with the blocking buffer provided in the kit for 1 h at room temperature. Subsequently, 150 µg of protein from each sample or 100 µl of serum was incubated with the array membranes overnight at 4 °C on a rocking platform. After washing, the membranes were incubated with a cocktail of biotinylated detection antibodies for 1 h at room temperature. The membranes were then washed again and incubated with streptavidin-HRP for 30 min. Chemiluminescent detection was performed via the prepared Chemi Reagent Mix in the kit, and the signals were captured via a chemiluminescence imager (MiniChemi 610 Plus, Beijing, China). Densitometric analysis was conducted via ImageJ software (NIH). The intensity of each cytokine

spot was normalized to that of the positive controls on the membrane, and the relative cytokine levels were quantified to those of the WT.

#### Western blotting

Protein extraction was performed via RIPA buffer (Beyotime, Shanghai, China) supplemented with protease and phosphatase inhibitors (Roche, Basel, Switzerland). The protein concentration was determined via a BCA protein assay kit (Epizyme Biotech, Shanghai, China). Equal amounts of protein (20 µg) were separated by SDS-PAGE on polyacrylamide gels and transferred to PVDF membranes (Millipore, Billerica, MA, USA). The membranes were blocked with 5% BSA in TBS-T (20 mM Tris-HCl, 150 mM NaCl, 0.1% Tween-20, pH 7.6) for 2 h at room temperature and incubated overnight at 4 °C with primary antibodies diluted in antibody dilution buffer (Beyotime, Shanghai, China). After being washed three times with TBS-T, the membranes were incubated with HRP-conjugated secondary antibodies (1:5000, Proteintech, Wuhan, China) for 2 h at room temperature and detected with a chemiluminescence detection system (Millipore). The primary antibodies used included the following: rabbit anti-STX12 monoclonal antibody (1:1000, custom-made), mouse anti-β-actin (1:5000; Proteintech, #60,008-1-Ig), mouse anti-GAPDH (1:20,000, Proteintech, #60,004-1-Ig), anti-OXPHOS antibody (1:1000; Abcam, #ab110413, Cambridge, UK), anti-cGAS (1:1000; Cell Signaling Technology, #31,659, Danvers, MA, USA), anti-TBK1(1:1000, Cell Signaling Technology, #3504S), anti-pTBK1(1:1000; Cell Signaling Technology, # 5483S), anti-IRF3(1:1000; Proteintech, #11,312-1-AP), anti-pIRF3(1:1000; Cell Signaling Technology, #29,047), anti-IL-6 (1:1000; Abcam, #ab229381), anti-S100A9 (1:1000; Boster, #PB0718, Wuhan, China). The grayscale intensity of the bands was analyzed using Fiji software.

#### RNA extraction and RT-qPCR

RNA samples were extracted via Trizol reagent (Invitrogen, Carlsbad, CA, USA) and RNA was converted to complementary deoxyribonucleic acid (cDNA) via a RevertAid First Strand cDNA Synthesis Kit following the manufacturer's instructions (Invitrogen). Quantitative reverse transcription-PCR (qRT-PCR) was performed via SYBR Green Master Mix (Takara, Otsu, Shiga, Japan) on the qTOWER<sup>3</sup> Series (Analytik Jena, Jena, Germany). Gene expression was calculated via the CT method relative to the housekeeping gene glyceraldehyde-3-phosphate dehydrogenase (GAPDH). The primers used for PCR were as follows:

Isg15: 5'-CTAGAGCTAGAGCCTGCAG-3'; 5'-AGT TAGTCACGGACACCAG-3';

Mx1: 5'- GGTCCAAACTGCCTTCGTAA -3'; 5'- TTC AGCTTCCTTTTCTTGGTTT -3';

Mx2: 5'- ACCAGGCTCCGAAAAGAGTT -3'; 5'- TCT CGTCCACGGTACTGCTT -3';

Ifi204: 5'- GGGAGTGGAAAATGGCACAAC -3'; 5'- TCAGCACCATCACTTGTTTGG -3';

Ifi2712a: 5'- CTGTTTGGCTCTGCCATAGGA -3'; 5'- TTCCTGCACAGTGGACTTGAC -3';

IL-6: 5'- CCGGAGAGGAGACTTCACAG -3'; 5'- TCC ACGATTTCACAGAGAAC -3';

CCL2: 5'- AAGAGGATCACCAGCAGCAG -3'; 5'- TCTGGACCCATTCTTCTTG -3';

CCL17: 5'- AGTGGAGTGTCCAGGGATG -3'; 5'- TGGCCTTCTTACATGTTTG -3';

CXCL10: 5'- CCAAGTGCTGCCGTCATTTTC -3'; 5'- GGCTCGCAGGGATGATTTCAA -3';

CCL20: 5'- TTTTGGGATGGAATTGGAC -3'; 5'- AGGTCTGTGCAGTGATGTGC -3'

CCL20: 5'- TTTTGGGATGGAATTGGAC -3'; 5'- AGGTCTGTGCAGTGATGTGC -3'

Ly6g: 5'- GACTTCCTGCAACACAACACTACC -3'; 5'- ACAGCATTACCAGTGATCTCAGT -3'

MPO: 5'- AGTTGTGCTGAGCTGTATGGA -3'; 5'- CGGCTGCTTGAAGTAAACAGG -3'

ELANE: 5'- CAGGAACTTCGTCATGTCAGC -3'; 5'- AGCAGTTGTGATGGGTCAAAG -3'

CSF3R: 5'- CCTCACTTGAACACCCAGG -3'; 5'- CCCTTGGTACTGACAGTCGG -3'

C3: 5'- CCAGCTCCCCATTAGCTCTG -3'; 5'- GCA CTTGCCTCTTTAGGAAGTC -3'

CXCL1: 5'- ACTGCACCCAAACCGAAGTC -3'; 5'- TGGGGACACCTTTTAGCATCTT -3'

CXCL2: 5'- CATCCAGAGCTTGAGTGTGACG -3'; 5'- GGCTTCAGGGTCAAGGCAAAC -3'

CXCL5: 5'- GTTCCATCTCGCCATTCATGC -3'; 5'- GCGGCTATGACTGAGGAAGG -3'

TNF: 5'- CCTGTAGCCCACGTCGTAG -3'; 5'- GGG AGTAGACAAGGTACAACCC -3'

Csf3: 5'- ATCCCGAAGGCTTCCCTGAGTG -3'; 5'- AGGAGACCTTGGTAGAGGCAGA -3'

#### Mitochondrial respiration in lung tissue homogenates

Pregnant *Stx12*<sup>+/-</sup> mice (HE) mice at gestational day 19.5 were humanely euthanized via cervical dislocation followed by immediate cesarean delivery. Fetuses were rapidly extracted and subjected to standardized neonatal resuscitation procedures including thorough drying, tactile stimulation for respiratory initiation, and continuous thermal support on a 37 °C pre-warmed pad. The intact lung tissues of fetal mice were carefully excised and placed in pre-chilled ice-cold PBS followed by twice rinse with PBS to eliminate blood contaminants. Preference was given to the smaller *Stx12*<sup>-/-</sup> mice. If immediate

processing was not possible, the tissue samples were stored in ice-cold BIOPS buffer (pH 7.1; 30 mM KCl, 10 mM KH<sub>2</sub>PO<sub>4</sub>, 0.6 mg/ml BSA, 5 mM MgCl<sub>2</sub>-6H<sub>2</sub>O, 1 mM EGTA, 105 mM K-MES). Approximately 15 mg of lung tissue was then homogenized in 1 ml MiR05 buffer (OROBOROS, 60,101-01) on ice using a glass homogenizer with 10 up-and-down strokes to generate a uniform homogenate.

Mitochondrial respiration was measured in duplicate under hyperoxic conditions at 37 °C using high resolution respirometry (Oxygraph-2 k, Oroboros Instruments, Innsbruck, Austria) with software (DatLab, version 4.2) that presents respiration in terms of oxygen rate (pmol/(s×mg)). The following protocol was applied: Basal oxygen consumption was measured for 10–15 min. Leak respiration was assessed by addition of pyruvate (P, 5 mM), glutamic acid (G, 10 mM) and malate (M, 2 mM), followed by adenosine diphosphate (ADP) (3 mM of magnesium (Mg<sup>2+</sup>) was added as well) to evaluate complex I linked respiratory capacity. Succinate (10 mM) was then added to measure complex I+II linked respiratory capacity, followed by the addition of rotenone inhibiting complex I to assess complex II linked respiratory capacity. 2.5 μM Antimycin A was added to inhibit complex III in the electron transport chain to measure the non-mitochondrial respiration rate. Finally, activators of complex IV, N, N, N', N'-Tetramethyl-p-phenylenediamine (TMPD) and ascorbate (As) were added to determine complex IV linked respiratory capacity. The subsequent reagent was added once the previous reagent had reached the plateau phase. Data from the plateau phase were collected for subsequent statistical analysis.

#### Primary culture of alveolar type II epithelial cells (AEC II)

The intact lung tissues of fetal mice (E19.5) were carefully excised and placed in pre-chilled ice-cold PBS. The residual tracheal and connective tissues were removed to ensure that only lung tissue was retained. The lungs were rinsed twice with prechilled ice-cold PBS and cut into approximately 1 mm<sup>3</sup> pieces using sharp ophthalmic scissors, while antibiotics was added during the cutting process. The lung tissue pieces were rinsed once with 0.25% trypsin (Gibco™; 25,200,072) (containing 0.01% DNase I (Sangon Biotech; A610099, Shanghai, China)) solution. The digestion was continued by pipetting the tissue with 0.25% trypsin (containing 0.01% DNase I) and the mixture was incubated at 37 °C in a shaking water bath for 10–20 min. The digestion process was terminated by adding an equal volume of DMEM/F12 medium (Gibco™; C11330500BT) containing 10% FBS (Gibco™; A5669701). The mixture was centrifuged at 1000 rpm for 8 min. The supernatant was discarded, and the cell pellet, which consisted mainly of AECs and fibroblasts, was

retained. The cell pellet was resuspended in 1 mL of 0.1% collagenase I solution (Sangon Biotech; A004214) and incubated at 37 °C with 5% CO<sub>2</sub> for 10–20 min (optimal duration 15 min). The digestion was terminated by adding an equal volume of DMEM/F12 medium containing 10% FBS, followed by thorough mixing with a pipette. After the cell suspension was filtered through a 200-mesh sieve, it was centrifuged at 1000 rpm for 5 min at low temperature, the supernatant was discarded, and the cell pellet, which primarily contained AECs and minimal fibroblasts, was collected. The cells were resuspended in 3 mL of red blood cell lysis buffer and incubated at room temperature for 10 min to lyse the erythrocytes. The mixture was centrifuged at 1000 rpm for 5 min at low temperature, the supernatant was discarded, and the cell pellet was resuspended in DMEM/F12 medium containing 10% FBS. The cells were cultured in a 55 cm<sup>2</sup> Petri dish at 37 °C with 5% CO<sub>2</sub>. After one hour, the adherent cells are primarily fibroblasts, whereas the nonadherent cells are mostly epithelial cells. The cells in the culture medium were gently aspirated and seeded into new culture plates. This process was repeated one hour later, and the remaining cells are primarily alveolar type II epithelial cells (AEC II). After 24 h, the culture medium was changed, and cell morphology and growth were observed under an inverted microscope.

#### **Immunostaining and confocal microscopy**

Cells were fixed with 4% FSB solution containing 4% paraformaldehyde (Servicebio; G1101, Wuhan, China) and 4% sucrose (Sangon Biotech; A610498) in PBS for 30 min at room temperature (RT) and then washed with PBS three times. The fixed cells were then exposed to 0.5% Triton X-100 and 5% serum in PBS for 30 min at RT for permeabilization and blocking. Next, the cells were incubated with the primary antibody overnight at 4 °C and diluted with 0.5% Triton X-100 and 5% serum in PBS. The primary antibodies used included the following: anti-TOM20 (1:500; Proteintech, # 11,802–1-AP) and anti-DNA (1:200; progen, # AC-30–10; Heidelberg, Germany). Following three washes with PBS, the cells were incubated with Alexa 488- and 555- conjugated secondary antibodies (Invitrogen; 1:500, # A21422; #A11008) for 1 h at RT and diluted with 0.5% Triton X-100 and 2% serum. The nuclei were then stained with DAPI (1:1000) for 10 min at RT. Finally, the coverslips were mounted with anti-fade reagent. Images were acquired on a Zeiss LSM 980 confocal microscope with Airyscan technology. To maintain clarity and uniformity throughout the paper, some images have been pseudocolored. For lung tissue immunostaining, the intact lung tissues of fetal mice (E19.5) were carefully excised and immersed in ice-cold 4% paraformaldehyde (PFA). After 24 h, the tissue was

transferred to 30% sucrose (Sangon Biotech; A610498), allowing the tissue to equilibrate until it sank, which usually takes 48–72 h. The precipitated lung tissue was removed, and the surface liquid was blotted with clean absorbent paper. The tissue was embedded in optimal cutting temperature (OCT) compound and rapidly frozen via dry ice or liquid nitrogen. The 30 µm sections were cut with a cryostat, and then stored at –20 °C or proceed directly with subsequent immunofluorescence staining. The sections were permeabilized in 0.1% Triton X-100 for 10 min at RT, followed by blocking with 3% BSA in PBS for an hour at RT. The antibody incubation process and image acquisition were similar to those used for the cells. The following primary antibodies were used: anti-TOM20 (1:500; Proteintech, # 11,802–1-AP), anti-DNA (1:200; progen, # AC-30–10; Heidelberg, Germany), anti-S100A9 (1:200; Boster; # PB0718) and anti-ly6g (1:100; BD Biosciences; # 551459). Images were acquired on a Zeiss LSM 980 confocal microscope with Airyscan or super-resolution imaging with HIS-SIM (High Sensitivity Structured Illumination).

#### **Image analysis**

Quantification of cytosolic DNA puncta was conducted using Fiji, a widely recognized software for image analysis in microscopy. The procedure involved the following steps: Initially, the regions corresponding to the cell nucleus were masked using Fiji to isolate the cytosolic compartment. Subsequently, the total number of cytosolic DNA puncta was determined using Fiji's analysis tools. Next, we quantified the cytosolic mtDNA puncta that co-localized with mitochondria using image calculator and analysis tools. We defined "cells with cytosolic mtDNA" as those with detectable free cytosolic DNA puncta, with a threshold of  $\geq 1$  punctum per cell.

#### **Detection of the mtDNA content in the cytosolic extracts**

Freshly purified lung alveolar type II epithelial cells were resuspended in 500 µl of buffer containing 150 mM NaCl, 50 mM HEPES pH 7.4 and 20 µg/ml digitonin (Sigma D141, St. Louis, MO, USA). The homogenates were incubated end-over-end for 10 min on a shaker to allow for selective plasma membrane permeabilization and then centrifuged three times at 800×g for 5 min to pellet intact cells. The supernatants were transferred to fresh tubes and centrifuged at 25,300×g for 10 min to pellet any remaining cellular chip, yielding cytosolic preparations free of nuclear, mitochondrial, and endoplasmic reticulum contamination. The protein concentrations of the samples were normalized via a BCA protein assay kit (Epizyme Biotech). DNA was extracted from equal amounts of cytosolic fractions using QIAquick Nucleotide Removal kit (QIAGEN,

Hilden, Germany) following the manufacturer's instructions. Quantitative PCR was performed on pure cytosolic fractions using mtDNA primers: mouse mtND2 forward, 5'-ccatcaactcaatctcactctatg-3', and reverse, 5'-gaactcctgtagtggtggaagg-3'; mouse cytochrome b (Cytb) forward, 5'-cttcgcttccacttcattacc-3', and reverse, 5'-ttgggtgtttgatcctgtttcg-3' and mouse Dloop1 forward, 5'-aatctaccatcctccgtgaaacc-3', and reverse, 5'-tcagtttagtaccaccaagttaa-3'. For each independent sample, qPCR was performed in triplicate.

#### Enzyme-linked immunosorbent assay (ELISA)

Lungs were collected from fetal mice (E19.5) and placed in ice-cold PBS to remove any residual blood. The tissues were then weighed and homogenized in ice-cold PBS with a protease inhibitor cocktail (Sigma-Aldrich, 11,836,170,001) using a homogenizer, with a buffer volume approximately ten times the tissue weight (e.g., 100 mg of tissue in 1 mL of buffer). The homogenate was centrifuged at 12,000×g for 10 min at 4 °C to pellet the cellular debris. The protein concentration of the lysate was measured via a BCA protein assay kit (Epizyme Biotech). ELISAs were performed according to the instructions of the mouse IL-1 $\beta$  ELISA kit (Protein-tech; KE10003) and the IFN- $\beta$  ELISA kit (E-EL-M0033), and the final concentrations were normalized to the respective protein concentrations.

#### Blood cell smear

Blood samples were collected from the mice via the decapitation method using heparinized capillary tubes to prevent coagulation. A small drop of blood (5–10  $\mu$ L) was then placed near one end of a clean microscope slide, and a thin, even smear was created by quickly and smoothly pulling a spreader slide across the stationary slide at a 30–45 degree angle. The blood smears were air-dried completely at room temperature, fixed in methanol for 2–3 min, and stained using Wright-Giemsa stain solution by immersing the slides for 10 min, rinsing with distilled water, and air drying. The stained blood smears were examined under a light microscope at 100× magnification using oil immersion. Differential white blood cell counts were performed by identifying and counting 100 leukocytes per slide, including neutrophils, lymphocytes and monocytes, and the total number of each cell type was recorded.

#### Quantification and statistical analysis

Student's t-test was used to analyze differences between two groups, and one-way or two-way ANOVA was used to analyze intergroup differences. *P*-values less than 0.05 were considered statistically significant. Statistical significance is displayed as \**p* < 0.05, \*\**p* < 0.01,

\*\*\**p* < 0.001, \*\*\*\**p* < 0.0001. The analysis was performed via GraphPad Prism 8 (GraphPad software). The densitometry results of western blotting were quantified via Fiji software. All the data are presented as the means  $\pm$  SEMs and other details such as the number of replicates and the level of significance, are mentioned in the figure legends and supplementary tables.

## Results

### The zebrafish model of *Stx12* knockdown

To gain insight into the function of *STX12* and the lethal mechanism associated with *STX12* deficiency, we developed a *Stx12* morpholino (MO) knockdown zebrafish model by embryonic injection of *Stx12*-targeting morpholinos. Two specific morpholino antisense strategies were employed to disrupt the zebrafish *Stx12* gene: one to block translation (ATG-MO) and the other to interfere with the proper splicing of exon 4 (E4I4-MO) (Figure S1A). The effectiveness of *Stx12* knockdown was validated by Sanger sequencing (Figure S1B) and qRT-PCR (Figure S1C).

Consistent with our previous findings that *Stx12* deficiency in mice was lethal, approximately 80% of *Stx12* morpholino-injected zebrafish embryos failed to survive beyond 6 h post fertilization (hpf), with only about 10% of these embryos could survive for days (Fig. 1A). This demonstrates that *Stx12* plays a vital role in the early development of embryos. The expression pattern of *Stx12* in zebrafish embryogenesis was subsequently explored. The representative images of five selected stages (0.2 hpf, 1 hpf, 2 hpf, 3.7 hpf, 6 hpf) were displayed in Fig. 1B, and quantitative RT-PCR for the embryo stages was performed (Fig. 1C), revealing the expression level of *Stx12* peaks within 2–3.7 h postfertilization during embryonic development, which led us to choose this time window for assessing the impact of *Stx12* knockdown.

### *STX12* deficiency induces the decrease of mitochondrial membrane potential but not apoptosis in zebrafish

Apoptosis and mitochondrial dysfunction play important roles in embryogenesis and tissue homeostasis [16, 17]. Acridine orange (AO) staining allows us to examine the role of *Stx12* in apoptosis [18, 19] while Tetramethylrhodamine methyl ester, perchlorate, biotium (TMRM) staining enables the investigation of the involvement of *STX12* in mitochondrial function [20]. The mitochondrial membrane potential ( $\Delta\Psi_m$ ) was estimated by monitoring fluorescence aggregates of TMRM [14, 15]. To assess the effectiveness of AO staining and TMRM staining in zebrafish embryos, wild-type (WT)-uninjected AB strain zebrafish embryos were exposed to different concentrations of AO (0.25, 0.5, 1.67 and 5  $\mu$ M) and TMRM (0.05, 0.1, 0.3 and 1  $\mu$ M) in fish water from

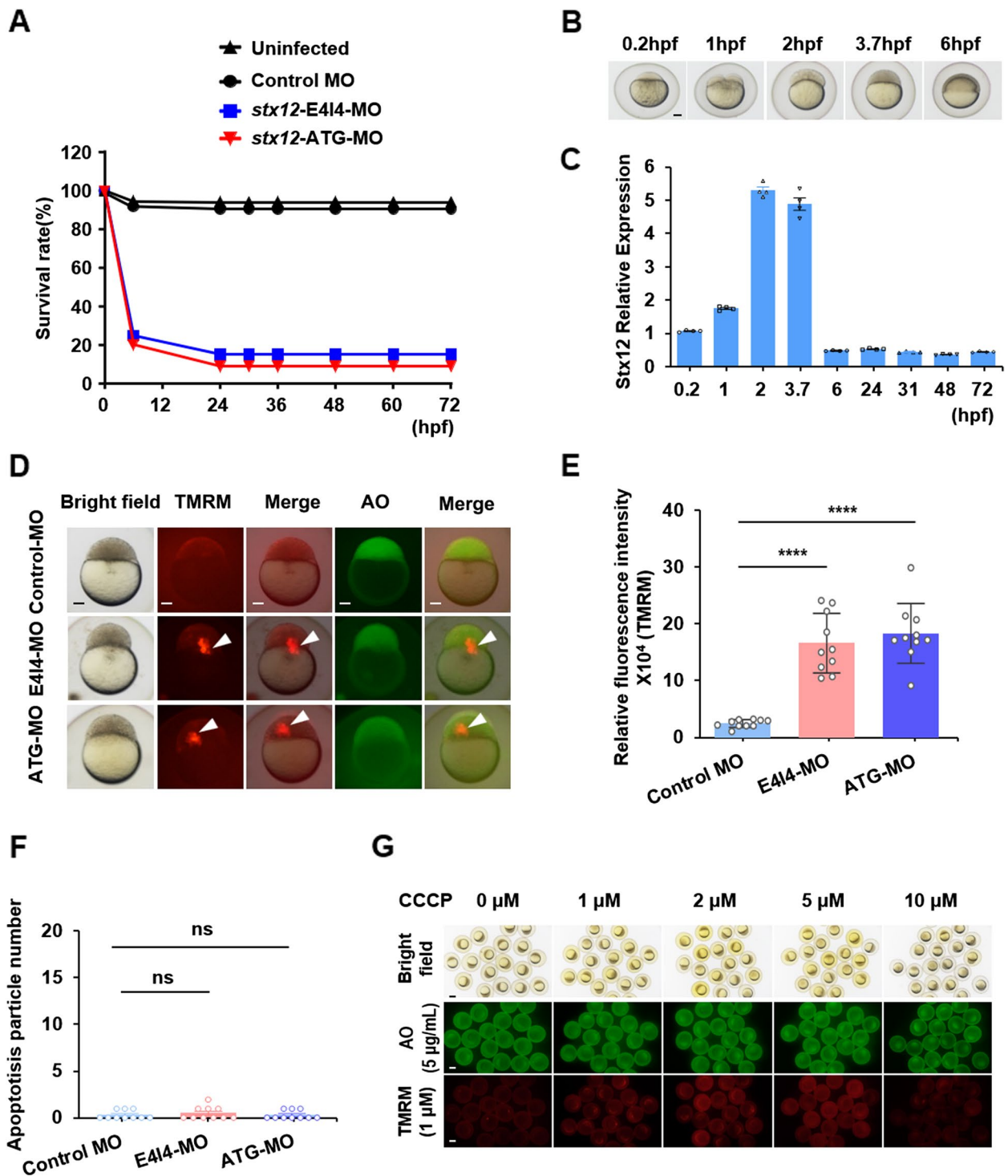


**Fig. 1** STX12 deficiency induces mitochondrial membrane potential defects in zebrafish. **A** A time-course plot of percent survival in the control vs. *Stx12* morphants for 3 days. dpf, days postfertilization; hpf, hours postfertilization. **B** Representative images of five selected stages of zebrafish embryos. Scale bar: 100  $\mu$ m. **C** qRT-PCR for five embryo development stages (0.2 hpf, 1 hpf, 2 hpf, 3.7 hpf and 6 hpf) demonstrating different expression patterns of *Stx12* during embryonic development. **D** Representative images of TMRM staining and AO staining in control, E4I4-MO and ATG-MO zebrafish. Treatment window: 2 hpf-3.7 hpf; Stage of image: 3.7 hpf. TMRM staining: 1  $\mu$ M; AO staining: 5  $\mu$ g/mL.  $n = 10$ , Scale bar: 100  $\mu$ m. **E** Quantification of the relative TMRM fluorescence intensity. **F** Quantification of apoptosis particle number in AO staining of control, E4I4-MO and ATG-MO zebrafish. Image analysis was performed using ImageJ software, with  $n = 10$  per group. **G** Representative images of TMRM staining and AO staining after CCCP treatment. Stage of Image: 3.7hpf. Scale bar: 300  $\mu$ m. Data are presented as mean  $\pm$  SEM; statistical significance was assessed by Student's *t*-test

2-hpf to 3.7-hpf at 28.5 °C in the dark, and the results demonstrated that 5 µg/ml AO and 1 µM TMRM yielded optimal fluorescence staining. In contrast, lower concentrations of TMRM and AO exhibited minimal fluorescence (Figure S2A). Accordingly, we stained zebrafish embryos with 5 µg/ml AO and 1 µM TMRM in fish water from 2-hpf to 3.7-hpf at 28.5 °C in the dark. Here, 1 µM TMRM was used in quenching mode, in which the fluorescence intensity was weaker as the probes accumulated in the mitochondria at high and quenching concentrations [21]. The representative images of AO staining and TMRM staining were present in Fig. 1D. Quantification of TMRM fluorescence intensity using Fiji software revealed a significant increase (approximately 5 to 10 fold) in embryos treated with ATG MO and 4I4 MO compared to the control-MO group (Fig. 1E). As shown in the TGF-MO induced apoptosis used as a positive control in Figure S3, apoptotic cells were visible as bright green spots while a less intense, homogeneous green signal was nonspecific background staining. In contrast, no apoptotic events were observed in embryos treated with ATG MO or 4I4 MO, compared to those treated with control-MO (Fig. 1D, F). These results indicate that *Stx12* knockdown in zebrafish does not induce apoptosis. Although TMRM quenching mode is a sensitive method for detecting rapid changes in  $\Delta\psi_m$  within individual cells, it is important to note that the release of TMRM from mitochondria can vary between different cell populations [22]. This variability may be influenced by differences in mitochondrial membrane potential, mitochondrial mass, and the presence of multidrug resistance transporters that can affect the retention of TMRM. In our study, we used zebrafish embryos at the same developmental stage, which helps to minimize variability due to differences in mitochondrial properties or cell types across different developmental stages. This consistency in developmental timing ensures that the cellular context and mitochondrial characteristics are relatively uniform across the embryos, thereby reducing the likelihood of differences in TMRM release rates between the wild-type (WT) and knockout (KO) cell populations. Besides, we performed control experiments to verify that the observed changes in TMRM fluorescence were

indeed reflective of changes in  $\Delta\psi_m$  rather than artifacts related to differences in mitochondrial mass or probe retention. We used Carbonyl cyanide 3-chlorophenylhydrazone (CCCP) to induce mitochondrial uncoupling and monitored the resulting changes in TMRM fluorescence in WT-uninjected zebrafish embryos. The increase of TMRM fluorescence intensity in embryos treated with ATG MO and 4I4 MO was similar and consistent with the effect of 1 µM CCCP (Fig. 1G). These findings indicated that *Stx12* knockdown in zebrafish promoted mitochondrial depolarization, resulting in a reduction in  $\Delta\psi_m$  with increased TMRM intensity in quenching mode. In addition, the toxicity and safety of CCCP in zebrafish model were also explored. The results indicated that 1 µM CCCP did not induce developmental delay or mortality in zebrafish embryos, suggesting the safety of the 1 µM CCCP concentration (Figure S4); conversely, 10 µM CCCP led to complete mortality in zebrafish embryos (Figure S4).

Collectively, our findings revealed that *Stx12* knockdown results in embryonic lethality and a reduction in the  $\Delta\psi_m$  in zebrafish.

#### STX12 deficiency elicits an inflammation response in mice, with inflammation being predominantly localized in the lung tissue

To investigate whether the function of STX12 is conserved across different species and to bridge studies from lower to higher organisms, building on the observation of impaired mitochondrial membrane potential in zebrafish embryos, we aimed to explore whether a similar phenotype occurs in a mouse model. To this end, we cocultured primary mouse embryo fibroblasts from *Stx12*<sup>-/-</sup> mice and their littermate controls (E17.5) and evaluated the mitochondrial membrane potential using 50 nM TMRM staining (unquenching mode) (Fig. 2A). The *Stx12*<sup>-/-</sup> MEFs were tagged with an EGFP fluorescent marker, which was incorporated during the gene editing process, serving as an indicator for *Stx12* knockout MEFs. In agreement with the findings in zebrafish, the mitochondrial membrane potential of MEFs from *Stx12*<sup>-/-</sup> mice was lower than that of those from littermate controls,

(See figure on next page.)

**Fig. 2** The loss of STX12 elicits an inflammatory response predominantly in lung tissue. **A** Representative images of TMRM staining (50 nM) of MEFs from *Stx12*<sup>-/-</sup> mice and littermate controls. **B** Quantification of the relative TMRM fluorescence intensity normalized to WT. The results are presented as the mean ± SEM; statistical significance was assessed by Student's t-test. **C, D** The cytokine kit displays of serum from *Stx12*<sup>-/-</sup> mice (HO) and the littermate controls (WT, *Stx12*<sup>+/+</sup>) (R&D Systems, Catalog # 410-MT) and quantitative analysis. **E, F** The cytokine kit displays of lung lysates from *Stx12*<sup>-/-</sup> mice (HO) and the littermate controls (WT, *Stx12*<sup>+/+</sup>) (R&D Systems, Catalog # 410-MT) and quantitative analysis. **G, H** The cytokine kit displays of brain lysates from *Stx12*<sup>-/-</sup> mice (HO) and the littermate controls (WT, *Stx12*<sup>+/+</sup>) (R&D Systems, Catalog # 410-MT) and quantitative analysis. The *Stx12*<sup>-/-</sup> mice and their littermate controls were obtained at embryonic day 19.5 (E19.5)

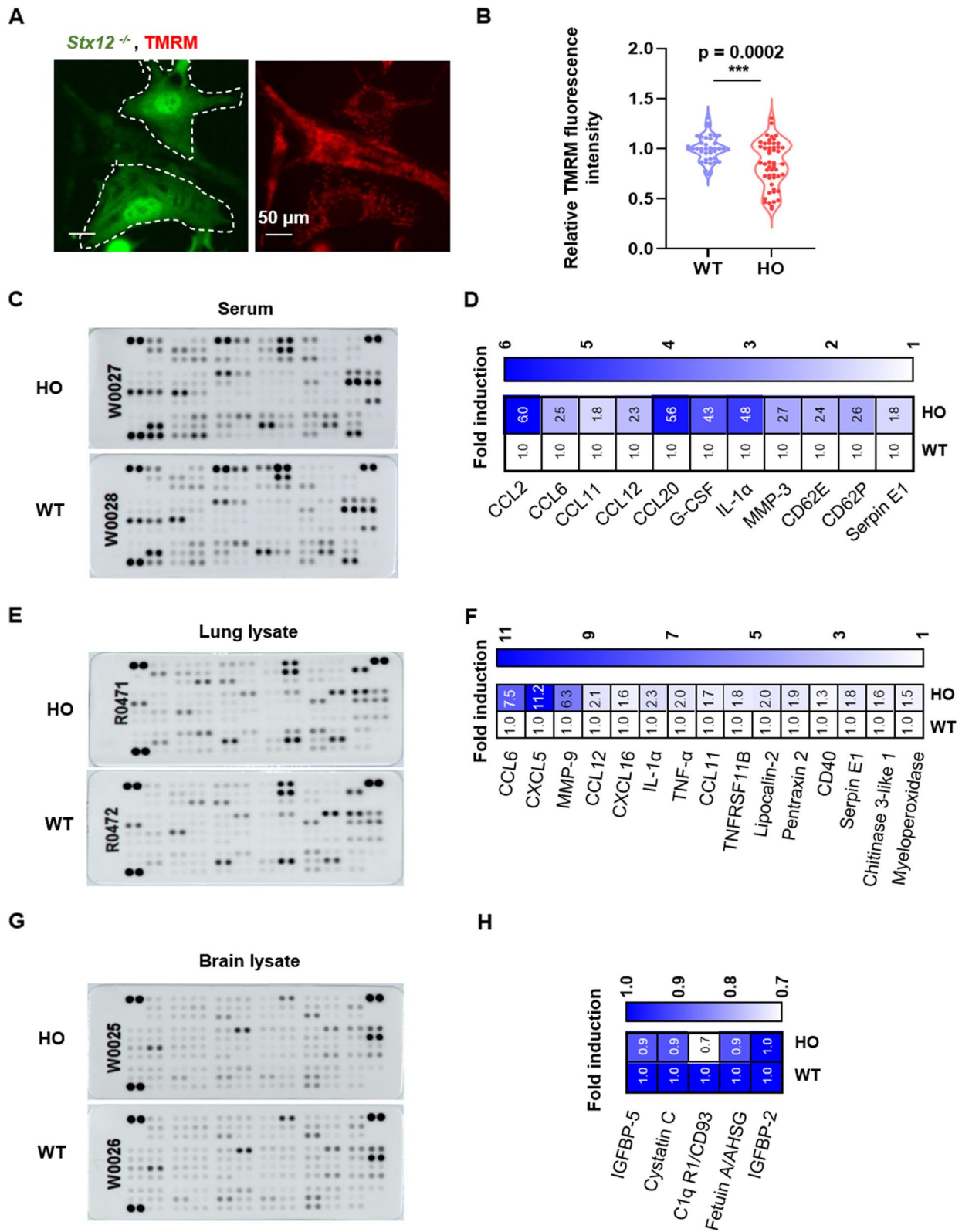


**Fig. 2** (See legend on previous page.)

as indicated by decreased TMRM fluorescence intensity (Fig. 2B).

In addition, based on its pale, swollen, and stiff phenotype as demonstrated in our previous study [13], we speculated that inflammation was activated in *Stx12*<sup>-/-</sup> mice. Therefore, we performed a cytokine array (Fig. 2C) to evaluate the expression of inflammatory cytokines in the serum of *Stx12*<sup>-/-</sup> (HO) and the littermate control (WT) mice (E19.5). The results revealed that *Stx12*<sup>-/-</sup> mice presented significantly elevated levels of several inflammatory cytokines, including chemokines (CCL2, CCL6, CCL11, CCL12, CCL20), cytokines (G-CSF, IL-1 $\alpha$ ), adhesion molecules (CD62E, CD62P), serpin E1, and MMP-3, in line with our initial hypothesis (Fig. 2D). To further investigate the tissue-specific origins of inflammation, we assessed cytokine expression levels in homogenates from multiple tissues including lung (Fig. 2E), brain (Fig. 2G), spleen (Figure S5A), liver (Figure S5C) and kidney (Figure S5E). The statistical results unveiled a significant activation of inflammation in the lung tissue (Fig. 2F), only few cytokines that appeared to show differences in the brain lysate (Fig. 2H) and minor increases in the lysates of the spleen (Figure S5B), liver (Figure S5D), and kidney (Figure S5F). The results highlighted that the lung was the primary site of inflammation, guiding our research aim accordingly.

Next, we performed bulk RNA sequencing (RNA-seq) of lung tissues from *Stx12*<sup>-/-</sup> mice and their littermate controls at E19.5. The gene expression profiles of the HO (*Stx12*<sup>-/-</sup>) and WT groups identified 13,340 co-expressed genes, 597 genes specifically expressed in the HO group, and 273 genes specifically expressed in the WT group (Figure S6A). The differentially expressed genes (DEGs) between the two groups were also analyzed. We defined DEGs with an absolute log-fold change above 1 and an FDR-adjusted *p*-value of less than 0.05,

yielding differences in 901 genes between HO and WT mice with 806 genes upregulated and 95 genes downregulated, and the volcano plot was shown in Figure S6B. GO enrichment analysis of the differentially upregulated genes revealed several significantly enriched terms within the biological process (BP), molecular function (MF), and cellular component (CC) categories and the top 10 pathways from the three enriched terms were plotted according to their Gene Ratios, as illustrated in the bubble plot (Figure S6C). The prominent categories were associated primarily with the regulation of the inflammatory response, leukocyte migration and cytokine activity, consistent with the inflammatory activation observed in the cytokine array of lung lysates from *Stx12*<sup>-/-</sup> mice.

### The deficiency of STX12 triggers mitochondrial damage and mitochondrial DNA release into the cytosol in alveolar type II epithelial cells

Building on the decreased membrane potential phenotype we observed in *Stx12*-knockdown zebrafish embryos and *Stx12*-knockout mouse MEFs, we further explored the effects of STX12 deficiency on the mitochondria of lung tissue. Considering that mitochondria generate most of the energy of the cell through oxidative phosphorylation (OXPHOS), we examined the expression levels of OXPHOS subunits in the lung tissue of *Stx12*<sup>-/-</sup> mice and their littermate controls via western blotting, with quantification conducted via ImageJ (Fig. 3A, B). Our analysis revealed a significant reduction in the expression levels of mitochondrial complex subunits I, II, and V in *Stx12*<sup>-/-</sup> mice compared with their littermate controls (E19.5), while the levels of subunits III and IV did not significantly change. Moreover, we assessed the mitochondrial oxygen consumption rate (OCR) of lung tissue homogenates from E19.5 mice of different genotypes using the O2K system, a widely used tool for measuring

(See figure on next page.)

**Fig. 3** The ablation of STX12 triggers mitochondrial damage and cytosolic release of mitochondrial DNA in alveolar type II epithelial cells.

**A** SDS-PAGE of mitochondrial OXPHOS subunits in lung lysates using OXPHOS cocktail antibodies. **B** Quantification of the levels of C I (complex I), C II (complex II), C III (complex III), C IV (complex IV) and C V (complex V) in Fig. 3A. The results are presented as the mean  $\pm$  SEM; statistical significance was assessed by Student's *t*-test. **C** Summarized data for the oxygen consumption capacity measured by high-resolution respirometry in Basal, C I leak, C I (complex I OXPHOS), C I + II (complex I + II OXPHOS), C II (complex II OXPHOS) and C IV (complex IV OXPHOS) (WT *n* = 5, HE *n* = 6, HO *n* = 4). **D** Volcano plots of the GSEA results, highlighting the differentially regulated pathways in *Stx12*<sup>-/-</sup> mouse lung tissue. FDR, false discovery rate; NES, normalized enrichment score. **E** Representative confocal images of immunofluorescence of primary alveolar type II epithelial cells (AEC II cells) using antibodies against TOMM20 (mitochondria) and DNA. (WT *n* = 4; KO *n* = 3 independent cultures) Boxes mark the enlarged images shown right. **F** The mean aspect ratio (ratio of the long axis to the short axis) of mitochondria per cell in AECII of *Stx12*<sup>-/-</sup> mice (HO) versus the littermate controls (WT). WT *n* = 23, HO *n* = 40. Results are presented as mean  $\pm$  SEM; statistical significance was assessed by Student's *t*-test. **G** The mean form factor of mitochondria per cell in AECII of *Stx12*<sup>-/-</sup> mice (HO) versus the littermate controls (WT). WT *n* = 23, HO *n* = 40. Results are presented as mean  $\pm$  SEM; statistical significance was assessed by Student's *t*-test. **H, I** Quantification of DNA foci: Number of cytosolic DNA foci per cell (**H**) and percentage of AEC II cells showing cytosolic DNA foci (**I**) from **E**. WT *n* = 3 HO *n* = 4 independent experiments. The results are presented as the mean  $\pm$  SD; statistical significance was assessed by Student's *t*-test. **J** Quantification of mtDNA copy number by qPCR using mtND2, CytB and Dloop1 primers, from isolated cytosolic fractions of AEC II cells of WT and *Stx12*<sup>-/-</sup> mice. The *Stx12*<sup>-/-</sup> mice and their littermate controls were obtained at embryonic day 19.5 (E19.5)

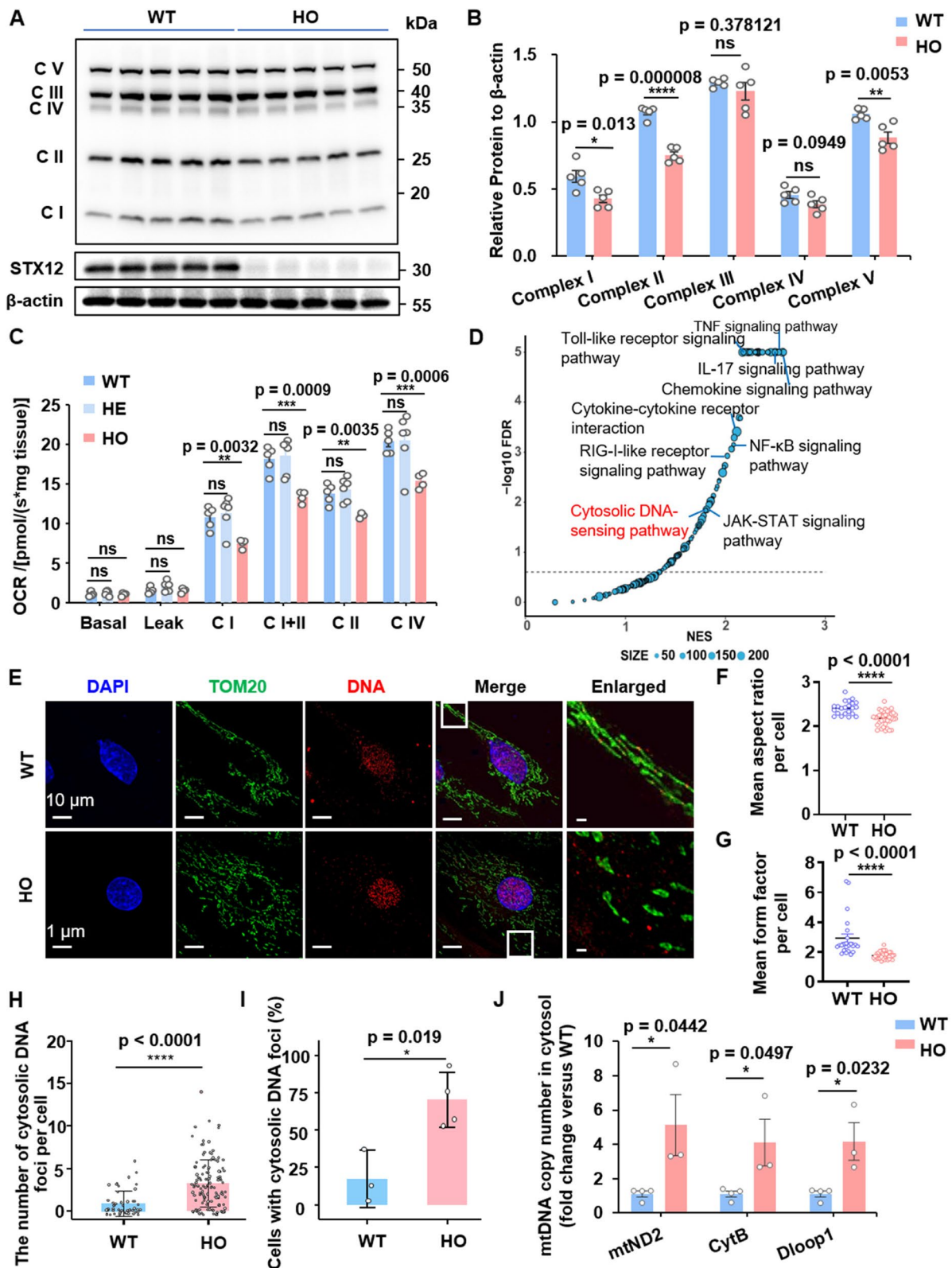


**Fig. 3** (See legend on previous page.)

mitochondrial respiration and assessing mitochondrial function in various tissues. After reaching baseline levels, we sequentially added the following compounds: 1. NAD<sup>+</sup>-linked substrates: Pyruvate (P) + Glutamic (G) + Malate (M); 2. Activator of ATP synthase: adenosine diphosphate (ADP + MgCl<sub>2</sub>); 3. Activator of complex II: succinate (S); 4. Inhibitor of complex I: rotenone (Rot); 5. Inhibitor of complex III: antimycin A (Ama); 6. Activators of complex IV: N, N, N', N'-Tetramethyl-p-phenylenediamine (TMPD) and Ascorbate (As). The subsequent reagent was added once that the previous treatment had reached the plateau phase. The resulting platform values corresponded to distinct mitochondrial functional parameters as indicated above the curve. The representative traces of samples from littermate *Stx12*<sup>-/-</sup> mice (HO) and controls (WT) were depicted in Figure S7. Statistical analysis of the OCR data revealed that the homozygous absence of *Stx12* led to a reduction in the OXPHOS levels of mitochondrial complex I, II, and IV in lung tissue. In contrast, no significant differences were observed between the HE and WT mice (Fig. 3C). Besides, we performed gene set enrichment analysis (GSEA) on the RNA-seq data mentioned before. GSEA, by analyzing gene sets, reduces the number of comparisons and enhances the statistical power to detect meaningful biological signals by aggregating the effects of genes within a pathway or functional group while traditional analyses like differential expression focus on individual genes and may suffer from multiple testing problems, leading to false positives. By analyzing gene sets that correspond to known pathways or biological functions, GSEA can reveal pathway-level effects, even when individual genes within the pathway might not show significant expression changes on their own. The results revealed that the most prevalent altered biological processes were associated with pathways linked to inflammation and the innate immune response in the lung tissue of *Stx12*<sup>-/-</sup> mice. Additionally, there was notable enrichment of the cytosolic DNA-sensing pathway (Fig. 3D). Next, we cultured primary alveolar type II epithelial cells (AEC II) and performed immunofluorescence staining using DNA-specific antibody to detect cytosolic DNA, and TOM20 antibody to identify mitochondria (Fig. 3E). We observed a notable change in the mitochondrial morphology of AEC II cells in *Stx12*<sup>-/-</sup> mice (HO, E19.5). In contrast to the elongated mitochondria observed in the WT group, the HO group exhibited mitochondria with a fragmented, rounded appearance. Quantitative analyses of mitochondrial morphology including parameters such as count (Figure S8A), mean area (Figure S8B), perimeter (Figure S8C), aspect ratio (Fig. 3F) and form factor (Fig. 3G) per cell, were consistent with the observation. More importantly, we performed quantitative analysis

of cytosolic DNA puncta using Fiji and statistical analysis demonstrated a marked increase in the number of cytosolic DNA foci per cell, as well as a higher proportion of cells containing cytosolic DNA foci in AECs II isolated from *Stx12*<sup>-/-</sup> mice, compared to those from littermate controls (E19.5) (Fig. 3H, I). These findings suggested a significant accumulation of cytosolic DNA in the alveolar type II epithelial cells of *Stx12*<sup>-/-</sup> mice. Previous studies have demonstrated the involvement of mitochondrial DNA (mtDNA) and mitochondrial RNA (mtRNA) as potent triggers of nucleic acid-sensing pathways, resulting in the activation of different inflammatory pathways [23]. In light of the observed mitochondrial abnormalities, we hypothesized that the cytosolic DNA foci might originate from the release of mitochondrial DNA (mtDNA). To explore this hypothesis, we first attempted and optimized a method for extracting purified cytoplasm. Based on the reviewed literature [24, 25], we employed two different protocols to isolate cytoplasm respectively from primary in vitro cultured AECII cells and freshly isolated AEC II cells from the fetal mice lung tissues at E19.5. The isolation efficiency was assessed by Western blot (WB) analysis, and purified cytoplasm was confirmed by two different methods as shown in Figure S9.

We quantified the copy number of mitochondrial DNA (mtDNA) in isolated cytosolic fractions of alveolar type II epithelial cells (AEC II) via quantitative polymerase chain reaction (qPCR) (Fig. 3J). In line with our hypothesis, the transcript levels of mitochondrial genes mt-ND2, mt-Cytb and mt-Dloop1 were significantly elevated in the cytosolic compartments of *Stx12*<sup>-/-</sup> alveolar type II epithelial cells, in comparison to the corresponding littermate controls.

These findings demonstrated that the knockout of *Stx12* resulted in impaired mitochondrial oxidative phosphorylation and the release of mtDNA into the cytoplasm, which might account for the activation of lung inflammation observed in *Stx12*<sup>-/-</sup> mice.

#### Loss of *Stx12* elicits activation of the cGAS-STING-TBK1 pathway and type I interferon pathway

In addition to detecting cytoplasmic DNA foci at the cellular level, these foci were also observed at the tissue level within the lung 30-micron frozen lung tissue sections obtained from *Stx12*<sup>-/-</sup> mice and the littermate controls (E19.5). The frozen lung tissue sections were stained with antibodies specific for DNA and TOM20, followed by imaging under fluorescence microscopy (Fig. 4A). The DNA foci that did not colocalize with TOM20 and DAPI were identified as cytoplasmic DNA. These foci were quantified and subjected to statistical analyses. Compared with the corresponding littermate controls,

*Stx12*<sup>-/-</sup> mice exhibited a significant increase in the number of cytoplasmic DNA foci per cell (Fig. 4B).

Previous extensive research has demonstrated that the cGAS-STING pathway (cyclic GMP-AMP synthase-stimulator of interferon genes) is a crucial component of the innate immune system and is responsible for detecting cytosolic DNA from various sources, including microbial pathogens, cancer cells, or DNA damage, and initiating an immune response [26–28]. Therefore, we hypothesized that activation of the cGAS-STING pathway might play a role in the observed phenotypes of *Stx12*-knockout mice. The results of western blotting revealed that *Stx12* knockout markedly increased the levels of cGAS and STING, and dramatically increased the phosphorylation of TBK1 and IRF3 in mouse lung lysates (Fig. 4C–F), suggesting the activation of the cGAS-STING signaling pathway in the lungs of *Stx12*<sup>-/-</sup> mice. Furthermore, enzyme-linked immunosorbent assay (ELISA) analysis revealed a statistically significant elevation in the level of IFN- $\beta$  within the lung tissue of *Stx12*<sup>-/-</sup> mice compared with that of control subjects (Fig. 4G). Moreover, among the up-regulated differential genes analyzed before, interferon-stimulated genes (ISGs) accounted for a substantial proportion, and the expression heatmap is shown in Fig. 4H. To confirm the upregulation of the expression of these ISGs including genes such as *Isg15*, *Mx2*, *Ifi204* and *Ifi2712a* in *Stx12*<sup>-/-</sup> mice, reverse transcription quantitative polymerase chain reaction (RT-qPCR) was used (Fig. 4I). Our findings illustrated the sequential activation of the interferon signaling pathway following the engagement of the cGAS-STING-pTBK1-pIRF3 cascade, providing a comprehensive understanding of the inflammatory response in *Stx12*<sup>-/-</sup> mice. Besides, we wonder if STX12 knockout induces activation of the cGAS-STING pathway in a broader context. Given the ease of obtaining and studying MEF cells, we also employed western blotting to assess the activation of the cGAS-STING pathway in *Stx12*-KO MEF cells (Figure S10A). The quantitative analysis revealed no significant changes in the levels of

cGAS, STING, or phosphorylated TBK1 in *Stx12*-KO MEF cells compared to wild-type controls, only with a modest upregulation of phosphorylated IRF3 (relative to total IRF3) (Figure S10B–I). The results suggested that the lung was particularly vulnerable to the deficiency of STX12. In summary, the cGAS-STING pathway and the Type I interferon signaling pathway were markedly activated by the presence of cytoplasmic mtDNA in the lung tissue of *Stx12*<sup>-/-</sup> mice.

#### Severe neutrophils-related immune response in *Stx12*-knockout mice

The Kyoto Encyclopedia of Genes and Genomes (KEGG) analysis is a valuable method for a mapping the results transcriptomic data to well-defined biological pathways, thereby facilitating the interpretation of gene expression changes within the context of cellular functions, metabolic processes, and disease mechanisms. By performing KEGG analysis on the upregulated differentially expressed genes identified from the RNA-seq data of lung tissue, we were able to gain deeper insights into the underlying biological processes. The analysis result revealed significant enrichment in inflammation-related pathways and the pathways with  $-\log_{10}(\text{padj}) > 5.5$  were displayed in Fig. 5A. Notably, the IL-17 signaling pathway and neutrophil extracellular trap (NET) formation pathway were prominently enriched, along with GO enrichment of neutrophil migration and neutrophil chemotaxis (Figure S6C), suggesting a crucial role of neutrophils in the pulmonary inflammatory response of *Stx12*<sup>-/-</sup> mice. Consistent with these findings, the blood smear results revealed a marked increase in the number of neutrophils (Fig. 5B) in *Stx12*<sup>-/-</sup> mice compared with *Stx12*<sup>+/+</sup> littermate controls, with no significant changes observed in lymphocytes or monocytes (Figure S11A and S11B). Moreover, qPCR analyses revealed upregulated expression of neutrophil markers, including *Ly6g*, myeloperoxidase (MPO), *ELANE* and *CSF3R*, as well as elevated levels of *CSF3*, *C3*, *CXCL1*, *CXCL2*, *CXCL5* and *TNF*,

(See figure on next page.)

**Fig. 4** The cGAS–STING pathway and Type I interferon pathway are activated in the lung tissue of *Stx12*<sup>-/-</sup> mice. **A** Representative confocal images of immunofluorescence of frozen lung slices (30  $\mu\text{m}$ ) using antibodies against TOMM20 (mitochondria) and DNA. White arrowheads indicate cytosolic DNA foci. Scale bar, 10  $\mu\text{m}$ . **B** Quantification of the average number of cytosolic DNA puncta per cell in the corresponding field. WT  $n=3$ , KO  $n=4$  independent experiments. **C** The expression of cGAS, STING, the phosphorylation of TBK1 (p-TBK1), the phosphorylation of IRF3 (p-IRF3) and GAPDH by western blot in lung lysates from *Stx12*<sup>-/-</sup> and the littermate control (WT, *Stx12*<sup>+/+</sup>) mice. **D** Relative quantification of cGAS and STING levels normalized to  $\beta$ -tubulin. **E** Relative quantification of p-TBK1 and p-IRF3 levels normalized to  $\beta$ -tubulin. **F** Quantification of the levels of p-TBK1/TBK1 and p-IRF3/IRF3. **G** IFN- $\beta$  levels of lung lysates from *Stx12*<sup>-/-</sup> and the littermate control (WT, *Stx12*<sup>+/+</sup>) mice ( $n=5$  per group) by enzyme-linked immunosorbent assay. **H** Heat map displays upregulated interferon stimulates genes (ISG) based on RNA-seq data of lung tissue. Rows represent individual ISGs and columns represent biological replicates. Color intensity reflects the level of gene expression and the values are represented as  $\log_2$  fold changes. **I** Expression levels of ISGs by qRT-PCR from the lung tissues of *Stx12*<sup>-/-</sup> ( $n=6$ ) and the littermate control (WT, *Stx12*<sup>+/+</sup>) ( $n=5$ ) mice. The mRNA expression of target genes was normalized to that of  $\beta$ -actin. The *Stx12*<sup>-/-</sup> mice and their littermate controls were obtained at embryonic day 19.5 (E19.5). The results are presented as the mean  $\pm$  SEM; statistical significance was assessed by Student's t-test

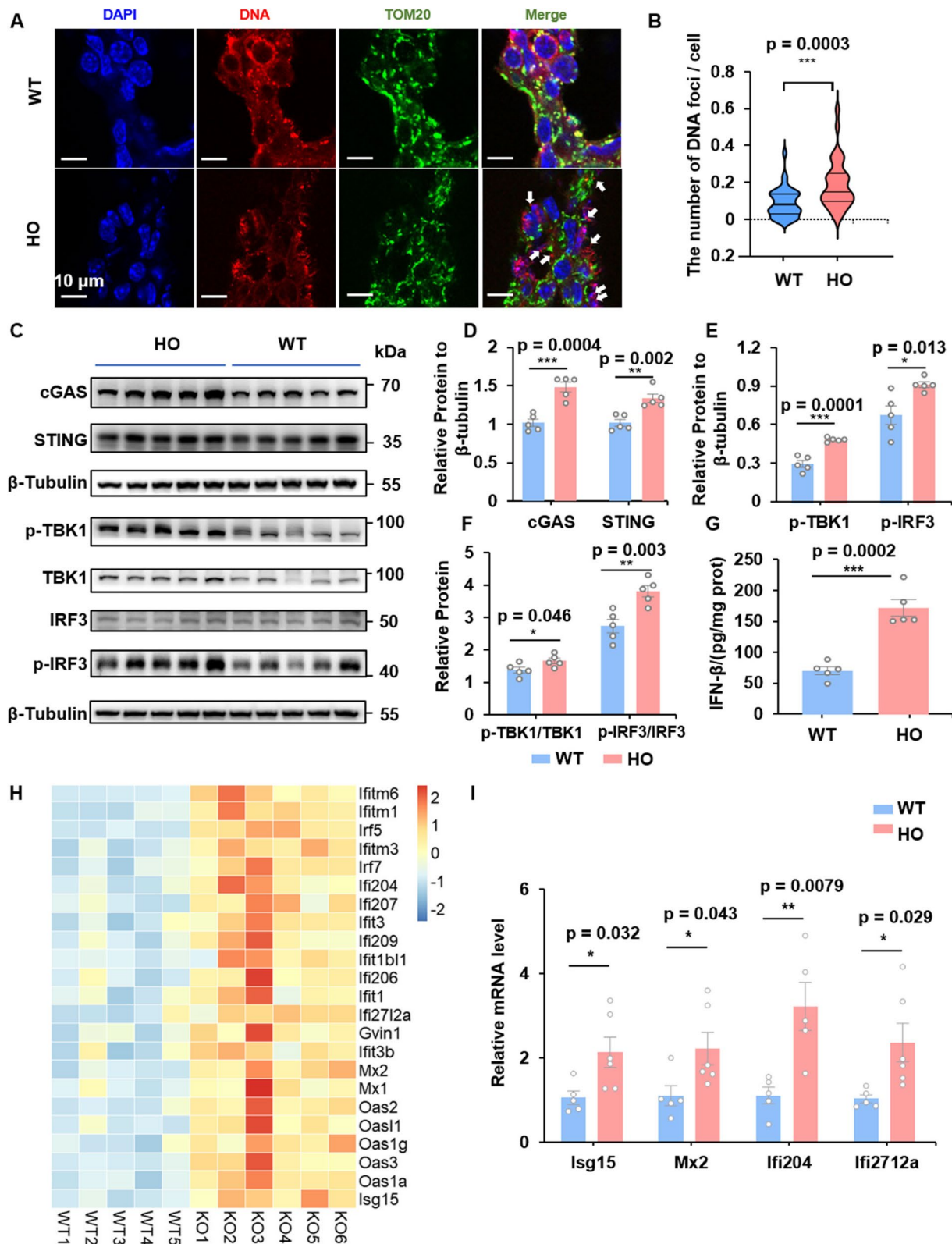


**Fig. 4** (See legend on previous page.)

which served as key chemokines for neutrophil recruitment and activation in the lung tissue of *Stx12*<sup>-/-</sup> mice compared with littermate controls (Fig. 5C). Meanwhile, we performed immunofluorescence staining on lung tissue with Ly6G and S100A9 antibodies (Fig. 5D). The statistical results demonstrated a significantly increase both in the overall fluorescence intensity and the fluorescence intensity per individual cell in the *Stx12*<sup>-/-</sup> mice compared to the littermate controls (Fig. 5E-H). S100A9, which is primarily secreted by neutrophils and can promote their migration and activation [29], was also found to be significantly upregulated by western blot analysis (Fig. 5I and J). These observations indicated pronounced neutrophil infiltration in the lung tissue of *Stx12*<sup>-/-</sup> mice. In addition, *Stx12*<sup>-/-</sup> lung homogenates showed increased IL-1 $\beta$  (Fig. 5K), which can activate neutrophils [30] and promote the formation of NETs [31]. Additionally, the upregulation of IL-6 was confirmed through qPCR and western blot analysis (Figs. 5I, J and L). The heatmap indicated the accumulation of various cytokines, including neutrophil-related elements, interleukins, TNF-related factors, complement component-related factors, colony-stimulating factors, and chemokines (Fig. 5M), in the lung tissue of *Stx12*<sup>-/-</sup> mice, with some further validated by qPCR (Figure S11C). These cytokines and granule enzymes (MPO, Elane and MMP) further attracted and activated neutrophils, creating a robust and cascading inflammatory response within the lung tissue of *Stx12*<sup>-/-</sup> mice. We hypothesized that this might be the cause of mortality in *Stx12* knockout mice. To investigate this, we also conducted rescue experiments using various interventions on pregnant mice, including the immunosuppressant, also the autophagy inducers rapamycin (intravenous injection; once a day; 1.6 mg/kg), the neutrophil elastase inhibitor sivelestat (intravenous injection; once a day; 50 mg/kg, DMSO 5%), immunomodulators vitamin C and vitamin D [32, 33] (via gavage; Vc: 205 mg/

kg in double distilled water; Vd: 150  $\mu$ g/kg in double distilled water, final ethanol < 1/10000), the voltage-dependent anion selective channel (VDAC) inhibitor VBIT-4 [34], inhibiting apoptosis and preventing mitochondrial dysfunction (provided in the drinking water; 20 mg/kg, final pH 5.0, DMSO 0.05%), the mitochondrial stabilizer taurine, protecting mitochondria from oxidative stress and maintaining normal mitochondrial function and energy metabolism (provided in the drinking water; 1000 mg/kg/day in double distilled water) and IFN inhibitor BX795, which exerts its effect by inhibiting TBK1 and IKK $\epsilon$  (5 mg/kg/day, administered intraperitoneally for 5 consecutive days). Given the lethality of *Stx12*-knockout mice at birth, these interventions cannot be administered directly to the knockout mice. The results showed that none of these interventions succeeded in rescuing the phenotype. However, sivelestat showed better effects than other treatments as demonstrated in the Figure S12, which was consistent with the potential role of neutrophile discussed above.

## Discussion

SNAREs constitute a critical family of proteins that facilitate the intricate process of membrane fusion within eukaryotic cells [35]. SNARE proteins are characterized by their ability to form a complex that brings the membranes of vesicles (v-SNARE) and target compartments (t-SNARE) into close proximity, facilitating the fusion process [36–39]. SNARE proteins are integral to numerous fundamental processes, including the initiation and extension of neurites, the specification and elongation of axons, as well as synaptogenesis and synaptic transmission [40, 41] and are critically implicated in a range of diseases such as neurodegenerative disorders, metabolic conditions [42] and cancer [43, 44].

As for the roles of SNARE proteins in mitochondrial dynamics, some evidence suggests that STX17 promotes

(See figure on next page.)

**Fig. 5** Neutrophils are involved in the severe inflammation in the lung tissue of *Stx12*<sup>-/-</sup> mice. **A** KEGG pathway analysis of the differentially upregulated expressed genes in *Stx12*<sup>-/-</sup> mice ( $-\log_{10}(\text{padj}) > 5.5$ ) from the RNA-seq data. **B** The number of neutrophils in the blood from *Stx12*<sup>-/-</sup> and the littermate control (WT, *Stx12*<sup>+/+</sup>) mice. **C** The relative mRNA levels of neutrophil markers (Ly6g, MPO, ELANE, and CSF3R) and key chemokines for neutrophil recruitment and activation (CSF3, C3, CXCL1, CXCL2, CXCL5, and TNF) normalized to those of  $\beta$ -actin. WT  $n=5$ , HO  $n=5$  independent samples. **D** Representative confocal images of immunofluorescence of frozen lung slice using antibodies against S100A9 and ly6g, the markers of neutrophils. Their increase of fluorescence intensity indicates the infiltration of neutrophils (WT  $n=4$ ; KO  $n=3$ ). **E, F** Quantification of the total fluorescence intensity of S100A9 and ly6g. It is relative to normalized WT intensity. **G, H** Quantification of fluorescence intensity of S100A9 and ly6g per cell. It is relative to normalized WT intensity. **I** Western blot analysis of the expression of IL-6, S100A9 and GAPDH in lung lysates from E19.5 *Stx12*<sup>-/-</sup> (HO) and the littermate control (WT, *Stx12*<sup>+/+</sup>) mice. **J** Relative quantification of IL-6 and S100A9 levels normalized to GAPDH. **K** IL-1 $\beta$  levels in the lung lysate from *Stx12*<sup>-/-</sup> ( $n=8$ ) and the littermate control (WT) mice ( $n=6$ ) at E19.5 by enzyme-linked immunosorbent assay. **L** Relative mRNA levels of IL-6 from lung lysates of *Stx12*<sup>-/-</sup> (HO) and the littermate control (WT) mice. **M** Heatmap showing upregulated inflammation-related genes including neutrophil-related gene, interleukins, tumor necrosis factor (TNF)-related genes, complement(C)-related genes, colony stimulating factor (CSF)-related genes and chemokines in *Stx12*<sup>-/-</sup> (HO) and the littermate control (WT) mice lung tissues. The values are represented as log<sub>2</sub> fold changes. The *Stx12*<sup>-/-</sup> mice and their littermate controls were obtained at embryonic day 19.5 (E19.5). The results are presented as the mean  $\pm$  SEM; statistical significance was assessed by Student's t-test

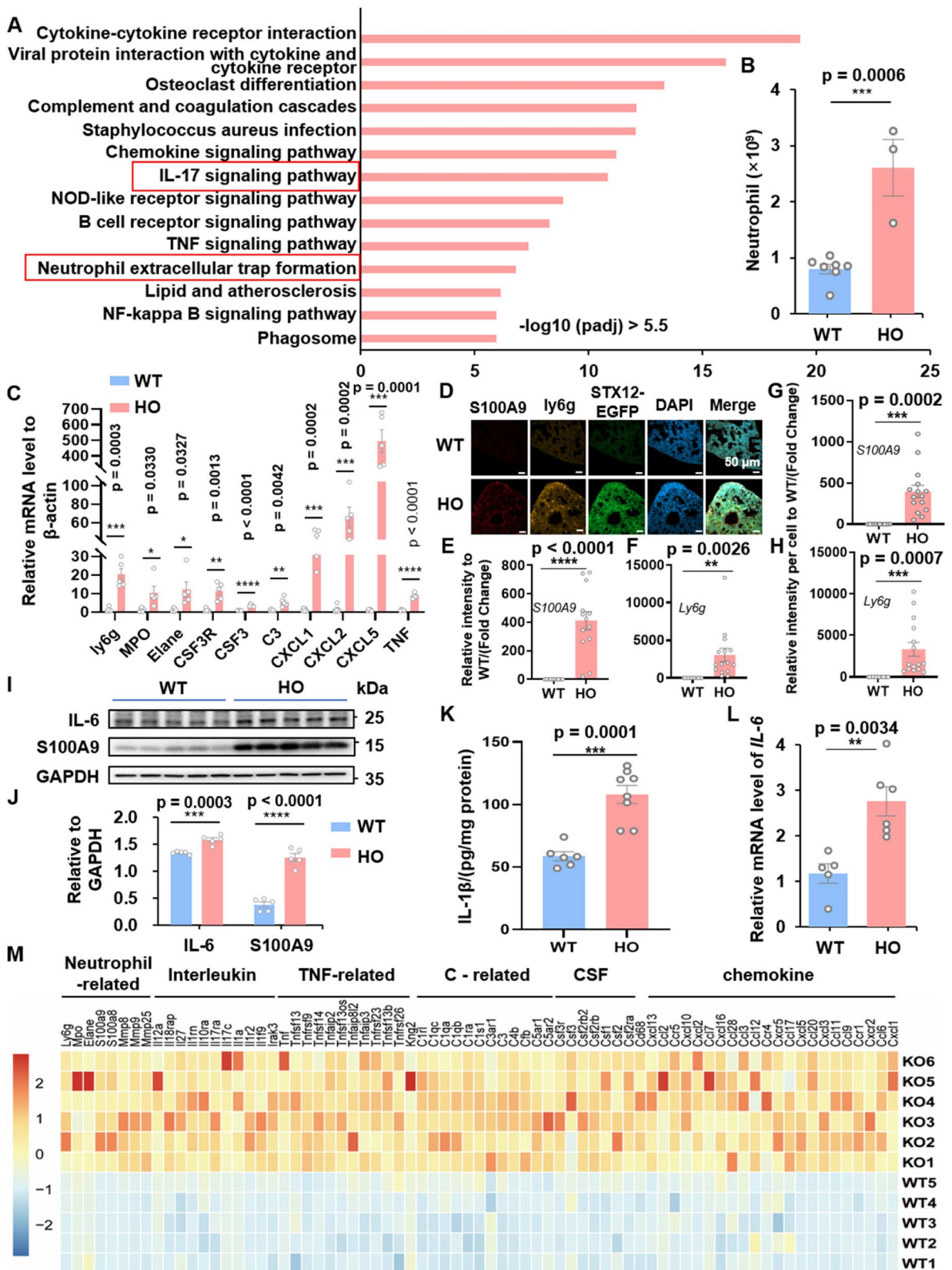
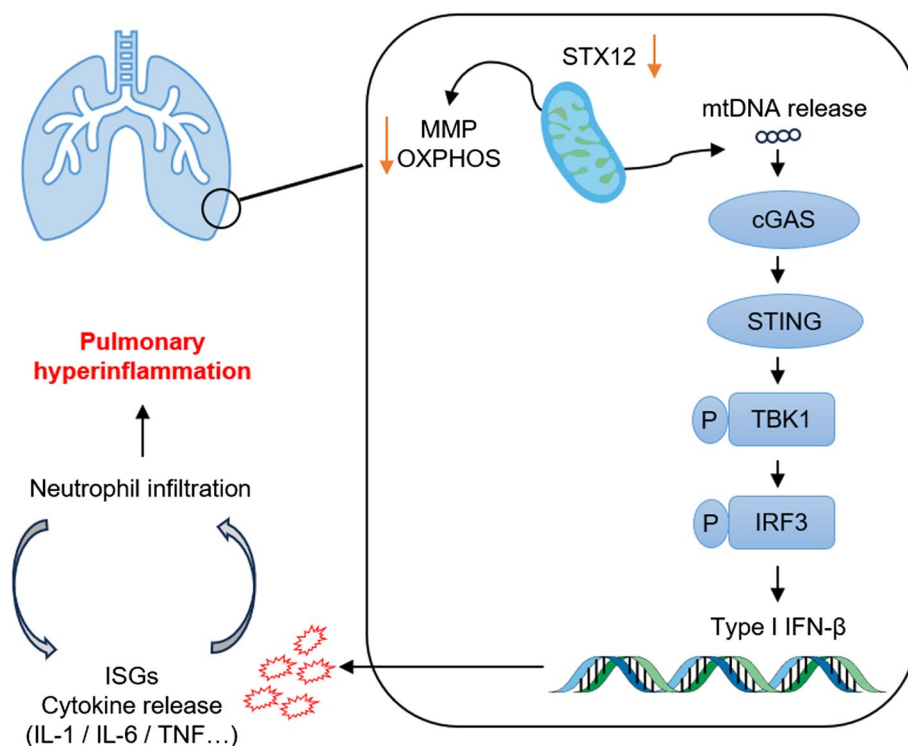


Fig. 5 (See legend on previous page.)

autophagy by localizing at contact sites between the endoplasmic reticulum and mitochondria [45] and is integral to the process of autophagosome maturation by mediating autophagosome-lysosome fusion and thus facilitating cellular homeostasis [46]. Syntaxin 4 (STX4), when enriched in skeletal muscle, reverses peripheral insulin resistance and ameliorates mitochondrial dynamics via the regulation of dynamin-related protein 1 (Drp1) [47] and plays a pivotal role in the lysosome-associated exocytosis of mitochondria, which is independent of mitophagy and contributes to the parkinsonism-like symptoms induced by flunarizine (FNZ) [48]. STX5 facilitates cholesterol trafficking from plasma membranes to mitochondria for adrenal steroid synthesis [49]. Furthermore, existing research has demonstrated that STX17 mitigates heart failure by promoting Drp1-dependent mitophagy via the recruitment of CDK1 [50] and plays a role in obesity cardiomyopathy through facilitating obesity-induced mitochondria-associated endoplasmic reticulum membranes (MAMs) formation and mitochondrial  $\text{Ca}^{2+}$  overload [51]. Here, we showed that STX12 depletion induced decreased mitochondrial membrane potential in zebrafish

(Fig. 1D and E) and mouse embryo fibroblasts (Fig. 2A and B). Moreover, *Stx12* knockdown led to reduced expression levels and OXPHOS levels of mitochondrial complex subunits and mtDNA release in lung tissue, activating the cGAS-STING signaling pathway and ultimately leading to pulmonary inflammation in mice (Fig. 6).

To our surprise, there is no significant changes in the levels of cGAS, STING, or phosphorylated TBK1 in *Stx12*-KO MEFs compared to wild-type MEFs, but a modest upregulation of phosphorylated IRF3 (relative to total IRF3) was observed in the knockout group, suggesting potential activation through a non-cGAS/STING pathway, such as the RIG-I pathway, as also indicated in Fig. 3D. This suggests that the activation of cGAS-STING pathway induced by *Stx12* knockout is tissue-specific in mice, with a particular sensitivity in lung tissue. As a member of the SNARE protein family, STX12 plays a crucial role in vesicular trafficking and plasma membrane fusion. Previous studies have reported that STX12 is colocalized with TFR in endosomes [52, 10], although the role of STX12 in endosomal dynamics remains unclear. Our previous research indicates that STX12 may regulate



**Fig. 6** Schematic of systemic immune-inflammation in *STX12*-KO mice. The ablation of *STX12* leads to decreased mitochondrial membrane potential (MMP), reduced expression levels of mitochondrial complex subunits, and the release of mitochondrial DNA (mtDNA). Then, mtDNA release activates the cGAS-STING-pTBK1-pIRF3 pathway, subsequently triggering Type I interferon response and downstream interferon-stimulated genes (ISGs) and cytokines in lung tissue. Additionally, cytokines release and neutrophil infiltration mutually enhance each other, resulting in an amplified cascade of hyperinflammation, referred to as “cytokine storm”, which potentially contributes to the mortality observed in *Stx12* knockout mice

endosomal membrane fusion, thereby facilitating rapid recycling of TFR and maintaining intracellular iron homeostasis [13]. In that study, we observed that *Stx12*-knockout (KO) mice exhibit iron deficiency anemia. Further investigation into the underlying mechanisms revealed that STX12 is critical for cellular iron transport and circulation. The absence of STX12 disrupts TFR cycling, leading to abnormalities in transferrin and iron homeostasis. Hemoglobin, the key molecule responsible for oxygen transport, requires iron for its synthesis. Iron deficiency directly impairs hemoglobin production, leading to reduced oxygen-carrying capacity. Organs sensitive to hypoxic conditions, which could result in mitochondrial depolarization and inflammatory responses. This may explain the observed tissue-specific effects in the lungs.

Terribly, the lack of cGAS-STING pathway activation in MEFs, along with the limitations that primary AECII cells are not suitable for long-term culture hinders further investigation of this pathway in vitro. Therefore, crossing *Stx12*<sup>+/−</sup> mice with cGAS-KO mice warrants further study to determine whether cGAS knockout rescues the phenotypes observed in *Stx12*<sup>−/−</sup> mice. Additionally, the broader impact of *Stx12* knockout on other tissues requires further investigation.

Transcriptome and inflammation analyses revealed the enrichment of cytokines and chemokines in *Stx12*<sup>−/−</sup> lung tissue. The enriched IL-17 signaling pathway has been implicated in the regulation of neutrophil function including migration, activation, and degranulation of these cells [53]. NETs are complex structures composed of DNA, histones, and antimicrobial proteins that are expelled by neutrophils as critical components of the immune response to ensnare and neutralize a broad spectrum of pathogens [54]. The formation of NETs is a highly regulated process that can be triggered by various stimuli, including IL-17. Once activated, neutrophils undergo a unique form of cell death that leads to the release of NETs, which can effectively immobilize and kill a wide range of microorganisms [55]. However, excessive or uncontrolled NET formation can also contribute to tissue damage and has been implicated in the pathogenesis of several inflammatory diseases, including acute lung injury and acute respiratory distress syndrome [56]. The substantial enrichment of the IL-17 signaling pathway and NET formation pathway in the KEGG analysis underscores the pivotal role of neutrophils in the pulmonary inflammation observed in *Stx12*-knockout mice (Fig. 5A). Furthermore, GO analysis, which emphasizes the chemotaxis and migration of

leukocytes—especially neutrophils—provides additional support for this conclusion (Figure S6C). For instance, Ly6G is a glycoprotein that is predominantly expressed on the surface of mouse neutrophils and is commonly used as a marker of neutrophils [57, 58]. MPO is a key enzyme found in the azurophilic granules of neutrophils and plays a crucial role in the antimicrobial defense of neutrophils by producing hypochlorous acid [59, 60]. Particularly, MPO has been implicated in the regulation of various neutrophil functions, including neutrophil activation [61, 62], trafficking [62, 63], phagocytosis [62], lifespan [64], the formation of extracellular traps [60] and MPO-triggered autoimmunity [62, 65]. Elane, also known as neutrophil elastase, is a serine protease enzyme found in the azurophilic granules of neutrophils. Elane has been shown to degrade almost all extracellular matrix proteins [66], disrupt the structural integrity of the tissue microenvironment [67], and induce the release of proinflammatory cytokines such as interleukin-6, interleukin-8 and so on [68, 69]. These significant elevations of Ly6G, MPO and Elane in *Stx12*<sup>−/−</sup> lung tissue indicate substantial neutrophil infiltration and potential damage of lung tissue. These injuries further exacerbate the release of cytokines and chemokines. S100A9, highly present in the cytoplasmic fraction of neutrophils, is associated with increased production of inflammatory cytokines [70] and can promote the migration and activation of neutrophils [29]. Besides, MMPs released by activated neutrophils have been demonstrated to modulate inflammatory responses by influencing the levels and activities of cytokines and chemokines, including the cleavage of several CXC chemokines in addition to degrading the extracellular matrix and facilitating neutrophil migration [71]. Furthermore, the increased cytokines such as IL-1, IL-6, TNF, CSF, C3 and neutrophil-specific chemokines, particularly CXCL1, CXCL2, and CXCL5 could also promote the chemotaxis and activation of neutrophils [72–76]. Besides, the significantly elevated IFN can indirectly influence neutrophil chemotaxis by modulating intracellular signaling pathways and the expression of extracellular chemokines, thereby exacerbating neutrophil infiltration. Therefore, we proposed that the infiltration of neutrophils and the release of cytokines in the lung tissue mutually enhance each other, creating a cascade amplification of inflammation, commonly referred to as "cytokine storm" [77, 78]. Consequently, we employed various interventions, but none effectively rescued the lethal phenotype. On the one hand, it is conceivable that the placental barrier significantly diminishes the fetal absorption of these drugs, which may account for the lack of efficacy observed.

The permeability of VBIT-4 through the placental barrier, in particular, remains uncertain. On the other hand, the observed lethality in the mice might result from a combination of systemic effects including multi-system failure, anemia, inflammation, and other potential complications. These findings suggest that the underlying mechanisms are complex and multifactorial, necessitating further detailed investigations to elucidate the precise causes of mortality in *Stx12*<sup>-/-</sup> mice.

To date, research on *Stx12* remains limited, with previous studies primarily focusing on its roles in endosomal trafficking, vesicle fusion, neuronal differentiation, and related processes. Our previous study explored the role of STX12 in TFR cycling, prompted by observations of iron-deficiency anemia in *Stx12*-knockout mice. Building on this previously identified lethal phenotype, our current study delves deeper into the function of STX12 in mitochondrial dynamics and immune inflammation. While we hypothesize that iron deficiency-induced hypoxia in lung tissue, which leads to mitochondrial stress, is a key factor, we cannot rule out the possibility that STX12 deficiency may also impair vesicle-mediated transport of mitochondrial membrane components or repair machinery, potentially affecting other tissues as well. The observed leakage of mtDNA suggests a potential failure in mitochondrial quality control mechanisms dependent on STX12-mediated vesicular transport. Further research is essential to fully elucidate the roles and mechanisms of STX12 in these processes.

Overall, the cGAS-STING activation triggered by pulmonary mtDNA release in *Stx12*<sup>-/-</sup> mice is a new mechanism of pulmonary inflammation, expanding our understanding of how mitochondria affect innate immune responses and providing a basis for further investigations of mitochondria injury-driven immunopathology.

### Supplementary Information

The online version contains supplementary material available at <https://doi.org/10.1186/s12964-025-02141-y>.

Supplementary Material 1

### Acknowledgements

This work is supported by the National Natural Science Foundation of China: JSK (32071137, 92054103). Funding for Scientific Research and Innovation Team of The First Affiliated Hospital of Zhengzhou University: JSK (ZYCXTD2023014).

### Authors' contributions

D.H.L. designed the experiments, performed the experiments, analyzed the data and wrote the manuscript. F.L. performed the preliminary exploration and part of the mouse experiments. R.Z.Y. discussed the project and provided help in the experimental design and data analysis. Z.B.W. performed the zebrafish experiments and data analysis. X.Y.M. and S.M.L. assisted with the experiments and manuscript writing. W.X.L., J.K.L., D.D.W. and R.Y.W. assisted with the experiments. S.A.L. and P.P.L. provided help in the experimental

design. J.S.K. developed the idea, directed the project and reviewed the paper. All the authors participated in discussions.

### Funding

This work is supported by the National Natural Science Foundation of China: JSK (32071137, 92054103). Funding for Scientific Research and Innovation Team of The First Affiliated Hospital of Zhengzhou University: JSK (ZYCXTD2023014).

### Data availability

The data (accession no. OMIX007643) reported in this paper have been deposited in the OMIX, China National Center for Bioinformatics/Beijing Institute of Genomics, Chinese Academy of Sciences (<https://ngdc.cnca.ac.cn/omix>).

### Declarations

#### Competing interests

The authors declare no competing interests.

Received: 6 November 2024 Accepted: 7 March 2025

Published online: 08 April 2025

### References

- Sørensen JB. SNARE complexes prepare for membrane fusion. *Trends Neurosci.* 2005;28:453–5.
- McNew JA. Regulation of SNARE-Mediated Membrane Fusion during Exocytosis. *Chem Rev.* 2008;108:1669–86.
- Rizo J, Chen X, Araç D. Unraveling the mechanisms of synaptotagmin and SNARE function in neurotransmitter release. *Trends Cell Biol.* 2006;16:339–50.
- Molecular RJ, Release MUN. *Annu Rev Biophys.* 2022;51:377–408.
- Prekeris R, Klumperman J, Chen YA, Scheller RH. Syntaxin 13 mediates cycling of plasma membrane proteins via tubulovesicular recycling endosomes. *J Cell Biol.* 1998;143:957–71.
- Sun W, Yan Q, Vida TA, Bean AJ. Hrs regulates early endosome fusion by inhibiting formation of an endosomal SNARE complex. *J Cell Biol.* 2003;162:125–37.
- Jani RA, Purushothaman LK, Rani S, Bergam P, Setty SRG. STX13 regulates cargo delivery from recycling endosomes during melanosome biogenesis. *J Cell Sci.* 2015;128:3263–76.
- Sarria FJ-C, Catsicas S, Hornung J-P, Hirling H. Developmental and spatial expression pattern of syntaxin 13 in the mouse central nervous system. *Cell Tissue Res* 2002; 309: 209–218.
- Hirling H, Steiner P, Chaperon C, Marsault R, Regazzi R, Catsicas S. Syntaxin 13 is a developmentally regulated SNARE involved in neurite outgrowth and endosomal trafficking. *Eur J Neurosci.* 2000;12:1913–23.
- Prekeris R, Foletti DL, Scheller RH. Dynamics of tubulovesicular recycling endosomes in hippocampal neurons. *J Neurosci.* 1999;19:10324–37.
- Kimura K, Mizoguchi A, Ide C. Regulation of growth cone extension by SNARE proteins. *J Histochem Cytochem.* 2003;51:429–33.
- Lu Y, Zhang Z, Sun D, Sweeney ST, Gao F-B. Syntaxin 13, a Genetic Modifier of Mutant CHMP2B in Frontotemporal Dementia, Is Required for Autophagosome Maturation. *Mol Cell.* 2013;52:264–71.
- Li F, Liu C-F, Xu Y-Z, Guo Y-L, Xue S-W, Kong X-D, et al. Neonatal lethality and recycling defect of transferrin receptor in mice with Syntaxin12/13 disruption. *Protein Cell.* 2019;10:67–71.
- Chazotte B. Labeling mitochondria with MitoTracker dyes. *Cold Spring Harb Protoc.* 2011;2011:990–2.
- He Y, Li W, Zheng Z, Zhao L, Li W, Wang Y, et al. Inhibition of Protein arginine methyltransferase 6 reduces reactive oxygen species production and attenuates aminoglycoside- and cisplatin-induced hair cell death. *Theranostics.* 2020;10:133–50.
- Abud HE. Shaping developing tissues by apoptosis. *Cell Death Differ.* 2004;11:797–9.
- Pinho BR, Santos MM, Fonseca-Silva A, Valentão P, Andrade PB, Oliveira JMA. How mitochondrial dysfunction affects zebrafish development

- and cardiovascular function: an in vivo model for testing mitochondria-targeted drugs. *Br J Pharmacol*. 2013;169:1072–90.
18. Chan P, Cheng S. Cadmium-induced ectopic apoptosis in zebrafish embryos. *Arch Toxicol*. 2003;77:69–79.
  19. Deng J, Yu L, Liu C, Yu K, Shi X, Yeung LWY, et al. Hexabromocyclodecane-induced developmental toxicity and apoptosis in zebrafish embryos. *Aquat Toxicol*. 2009;93:29–36.
  20. Meng X-Y, Wang D-D, Xie T-R, Yang R-Z, Liu C-F, Liu D-H et al. A sensitive mitochondrial thermometry 2.0 and the availability of thermogenic capacity of brown adipocyte. *Front Physiol* 2022; 13: 977431.
  21. Kang JH, Katsikis G, Li Z, Sapp KM, Stockslager MA, Lim D, et al. Monitoring and modeling of lymphocytic leukemia cell bioenergetics reveals decreased ATP synthesis during cell division. *Nat Commun*. 2020;11:4983.
  22. Brand MD, Nicholls DG. Assessing mitochondrial dysfunction in cells. *Biochem J*. 2011;435:297–312.
  23. Riley JS, Tait SW. Mitochondrial DNA in inflammation and immunity. *EMBO Rep*. 2020;21: e49799.
  24. Chen L, Dong J, Liao S, Wang S, Wu Z, Zuo M, et al. Loss of Sam50 in hepatocytes induces cardiolipin-dependent mitochondrial membrane remodeling to trigger mtDNA release and liver injury. *Hepatology*. 2022;76:1389–408.
  25. Zecchini V, Paupe V, Herranz-Montoya I, Janssen J, Wortel IMN, Morris JL, et al. Fumarate induces vesicular release of mtDNA to drive innate immunity. *Nature*. 2023;615:499–506.
  26. Regulation and function of the cGAS–STING pathway of cytosolic DNA sensing | *Nature Immunology*. <https://www.nature.com/articles/ni.3558> (Accessed 15 Jul 2024).
  27. M M, S P, Ka F. DNA sensing by the cGAS-STING pathway in health and disease. *Nature reviews Genetics* 2019; 20. <https://doi.org/10.1038/s41576-019-0151-1>.
  28. Hopfner K-P, Hornung V. Molecular mechanisms and cellular functions of cGAS-STING signalling. *Nat Rev Mol Cell Biol*. 2020;21:501–21.
  29. Catz SD. Divergent mechanisms of inflammasome activation in neutrophil early response and inflammation. *Nat Immunol*. 2023;24:1970–1.
  30. Hackel A, Aksamit A, Bruderek K, Lang S, Brandau S. TNF- $\alpha$  and IL-1 $\beta$  sensitize human MSC for IFN- $\gamma$  signaling and enhance neutrophil recruitment. *Eur J Immunol*. 2021;51:319–30.
  31. Lin S, Zhu P, Jiang L, Hu Y, Huang L, He Y, et al. Neutrophil extracellular traps induced by IL-1 $\beta$  promote endothelial dysfunction and aggravate limb ischemia. *Hypertens Res*. 2024;47:1654–67.
  32. Kang J. Vitamin intervention for cytokine storm in the patients with coronavirus disease 2019. *MedComm*. 2020;1:81–3.
  33. Jin A, Zhao Y, Yuan Y, Ma S, Chen J, Yang X, et al. Single Treatment of Vitamin D3 Ameliorates LPS-Induced Acute Lung Injury through Changing Lung Rodentibacter abundance. *Molecular Nutrition Food Res*. 2022;66:2100952.
  34. Kim J, Gupta R, Blanco LP, Yang S, Shteinfer-Kuzmine A, Wang K, et al. VDAC oligomers form mitochondrial pores to release mtDNA fragments and promote lupus-like disease. *Science*. 2019;366:1531–6.
  35. Jahn R, Cafiso DC, Tamm LK. Mechanisms of SNARE proteins in membrane fusion. *Nat Rev Mol Cell Biol*. 2024;25:101–18.
  36. Stanton AE, Hughson FM. The machinery of vesicle fusion. *Curr Opin Cell Biol*. 2023;83: 102191.
  37. Jahn R, Cafiso DC, Tamm LK. Mechanisms of SNARE proteins in membrane fusion. *Nat Rev Mol Cell Biol*. 2024;25:101–18.
  38. D U, Fm H. SNARE protein structure and function. Annual review of cell and developmental biology 2003; 19. <https://doi.org/10.1146/annurev.cellbio.19.110701.155609>.
  39. Jahn R, Scheller RH. SNAREs — engines for membrane fusion. *Nat Rev Mol Cell Biol*. 2006;7:631–43.
  40. Fl U, Sl G. SNARE-Mediated Exocytosis in Neuronal Development. *Frontiers in molecular neuroscience* 2020; 13. <https://doi.org/10.3389/fnmol.2020.00133>.
  41. Margiotta A. Role of SNAREs in Neurodegenerative Diseases. *Cells*. 2021;10:991.
  42. Dc T, Hy G. Recent Insights into Beta-cell Exocytosis in Type 2 Diabetes. *Journal of molecular biology* 2020; 432. <https://doi.org/10.1016/j.jmb.2019.12.012>.
  43. Williams KC, Coppolino MG. SNARE-dependent interaction of Src, EGFR and  $\beta$ 1 integrin regulates invadopodia formation and tumor cell invasion. *J Cell Sci*. 2014;127:1712–25.
  44. Meng J, Wang J. Role of SNARE proteins in tumorigenesis and their potential as targets for novel anti-cancer therapeutics. *Biochim Biophys Acta*. 2015;1856:1–12.
  45. Hamasaki M, Furuta N, Matsuda A, Nezu A, Yamamoto A, Fujita N, et al. Autophagosomes form at ER–mitochondria contact sites. *Nature*. 2013;495:389–93.
  46. An H-K, Chung KM, Park H, Hong J, Gim J-E, Choi H, et al. CASP9 (caspase 9) is essential for autophagosome maturation through regulation of mitochondrial homeostasis. *Autophagy*. 2020;16:1598–617.
  47. Merz KE, Hwang J, Zhou C, Veluthakal R, McCown EM, Hamilton A, et al. Enrichment of the exocytosis protein STX4 in skeletal muscle remediates peripheral insulin resistance and alters mitochondrial dynamics via Drp1. *Nat Commun*. 2022;13:424.
  48. Bao F, Zhou L, Zhou R, Huang Q, Chen J, Zeng S et al. Mitolysosome exocytosis, a mitophagy-independent mitochondrial quality control in flunarizine-induced parkinsonism-like symptoms. *Science Advances* 2022; 8: eabk2376.
  49. Deng B, Shen W-J, Dong D, Azhar S, Kraemer FB. Plasma membrane cholesterol trafficking in steroidogenesis. *FASEB J*. 2019;33:1389–400.
  50. Xu H, Wang X, Yu W, Sun S, Wu NN, Ge J, et al. Syntaxin 17 Protects Against Heart Failure Through Recruitment of CDK1 to Promote DRP1-Dependent Mitophagy. *JACC Basic Transl Sci*. 2023;8:1215–39.
  51. Xu H, Yu W, Sun M, Bi Y, Wu NN, Zhou Y, et al. Syntaxin17 contributes to obesity cardiomyopathy through promoting mitochondrial Ca<sup>2+</sup> overload in a Parkin-MCUB-dependent manner. *Metabolism*. 2023;143: 155551.
  52. Tang BL, Tan AE, Lim LK, Lee SS, Low DY, Hong W. Syntaxin 12, a member of the syntaxin family localized to the endosome. *J Biol Chem*. 1998;273:6944–50.
  53. Taylor PR, Roy S, Leal SM, Sun Y, Howell SJ, Cobb BA, et al. Activation of neutrophils by autocrine IL-17A-IL-17RC interactions during fungal infection is regulated by IL-6, IL-23, ROR $\gamma$ t and dectin-2. *Nat Immunol*. 2014;15:143–51.
  54. Brinkmann V, Reichard U, Goosmann C, Fauler B, Uhlemann Y, Weiss DS, et al. Neutrophil extracellular traps kill bacteria. *Science*. 2004;303:1532–5.
  55. Papayannopoulos V. Neutrophil extracellular traps in immunity and disease. *Nat Rev Immunol*. 2018;18:134–47.
  56. Qu M, Chen Z, Qiu Z, Nan K, Wang Y, Shi Y, et al. Neutrophil extracellular traps-triggered impaired autophagic flux via METTL3 underlies sepsis-associated acute lung injury. *Cell Death Discov*. 2022;8:1–13.
  57. Boivin G, Faget J, Ancey P-B, Gkasti A, Mussard J, Engblom C, et al. Durable and controlled depletion of neutrophils in mice. *Nat Commun*. 2020;11:2762.
  58. A H, M H, L M, F N, L B, M S et al. Catchup: a mouse model for imaging-based tracking and modulation of neutrophil granulocytes. *Nature methods* 2015; 12. <https://doi.org/10.1038/nmeth.3322>.
  59. Aratani Y. Myeloperoxidase: Its role for host defense, inflammation, and neutrophil function. *Arch Biochem Biophys*. 2018;640:47–52.
  60. Metzler KD, Fuchs TA, Nauseef WM, Reumaux D, Roesler J, Schulze I, et al. Myeloperoxidase is required for neutrophil extracellular trap formation: implications for innate immunity. *Blood*. 2011;117:953–9.
  61. Lau D, Mollnau H, Eiserich JP, Freeman BA, Daiber A, Gehling UM, et al. Myeloperoxidase mediates neutrophil activation by association with CD11b/CD18 integrins. *Proc Natl Acad Sci U S A*. 2005;102:431–6.
  62. Rizo-Téllez SA, Sekheri M, Filep JG. Myeloperoxidase: Regulation of Neutrophil Function and Target for Therapy. *Antioxidants*. 2022;11:2302.
  63. Klinke A, Nussbaum C, Kubala L, Friedrichs K, Rudolph TK, Rudolph V, et al. Myeloperoxidase attracts neutrophils by physical forces. *Blood*. 2011;117:1350–8.
  64. El Kebir D, József L, Pan W, Filep JG. Myeloperoxidase delays neutrophil apoptosis through CD11b/CD18 integrins and prolongs inflammation. *Circ Res*. 2008;103:352–9.
  65. Xiao H, Heeringa P, Hu P, Liu Z, Zhao M, Aratani Y, et al. Antineutrophil cytoplasmic autoantibodies specific for myeloperoxidase cause glomerulonephritis and vasculitis in mice. *J Clin Invest*. 2002;110:955–63.
  66. Havemann K, Gramse M. Physiology and Pathophysiology of Neutral Proteinases of Human Granulocytes. In: *Proteases*. Springer, Boston, MA, 1984, pp 1–20.
  67. Kawabata K, Hagio T, Matsuoka S. The role of neutrophil elastase in acute lung injury. *Eur J Pharmacol*. 2002;451:1–10.

68. Bédard M, McClure CD, Schiller NL, Francoeur C, Cantin A, Denis M. Release of interleukin-8, interleukin-6, and colony-stimulating factors by upper airway epithelial cells: implications for cystic fibrosis. *Am J Respir Cell Mol Biol*. 1993;9:455–62.
69. Nakamura H, Yoshimura K, McElvaney NG, Crystal RG. Neutrophil elastase in respiratory epithelial lining fluid of individuals with cystic fibrosis induces interleukin-8 gene expression in a human bronchial epithelial cell line. *J Clin Invest*. 1992;89:1478–84.
70. Sprenkeler EGG, Zandstra J, van Kleef ND, Goetschalckx I, Verstegen B, Aarts CEM, et al. S100A8/A9 Is a Marker for the Release of Neutrophil Extracellular Traps and Induces Neutrophil Activation. *Cells*. 2022;11:236.
71. Van Den Steen PE, Wuyts A, Husson SJ, Proost P, Van Damme J, Opdenaker G. Gelatinase B/MMP-9 and neutrophil collagenase/MMP-8 process the chemokines human GCP-2/CXCL6, ENA-78/CXCL5 and mouse GCP-2/LIX and modulate their physiological activities. *Eur J Biochem*. 2003;270:3739–49.
72. Zimmermann M, Aguilera FB, Castellucci M, Rossato M, Costa S, Lunardi C, et al. Chromatin remodelling and autocrine TNF $\alpha$  are required for optimal interleukin-6 expression in activated human neutrophils. *Nat Commun*. 2015;6:6061.
73. Lin S, Zhu P, Jiang L, Hu Y, Huang L, He Y, et al. Neutrophil extracellular traps induced by IL-1 $\beta$  promote endothelial dysfunction and aggravate limb ischemia. *Hypertens Res*. 2024;47:1654–67.
74. Baggiolini M, Dewald B, Moser B. Human Chemokines: An Update. *Annu Rev Immunol*. 1997;15:675–705.
75. Wolpe SD, Cerami A. Macrophage inflammatory proteins 1 and 2: members of a novel superfamily of cytokines. *FASEB J*. 1989;3:2565–73.
76. Matsukawa A, Hogaboam CM, Lukacs NW, Lincoln PM, Strieter RM, Kunkel SL. Endogenous monocyte chemoattractant protein-1 (MCP-1) protects mice in a model of acute septic peritonitis: cross-talk between MCP-1 and leukotriene B4. *J Immunol*. 1999;163:6148–54.
77. Karki R, Kanneganti T-D. The 'cytokine storm': molecular mechanisms and therapeutic prospects. *Trends Immunol*. 2021;42:681–705.
78. Borges L, Pithon-Curi TC, Curi R, Hatanaka E. COVID-19 and Neutrophils: The Relationship between Hyperinflammation and Neutrophil Extracellular Traps. *Mediators Inflamm*. 2020;2020:8829674.

### Publisher's Note

Springer Nature remains neutral with regard to jurisdictional claims in published maps and institutional affiliations.